Focus Section: EarthScope Alaska and Canada

Imaging the Tectonic Grain of the Northern Cordillera Orogen Using Transportable Array Receiver Functions

Vera Schulte-Pelkum[*1], Jonathan Saul Caine[2], James V. Jones, III[3], and Thorsten W. Becker[4]

Abstract

Azimuthal variations in receiver function conversions can image lithospheric structural contrasts and anisotropic fabrics that together compose tectonic grain. We apply this method to data from EarthScope Transportable Array in Alaska and additional stations across the northern Cordillera. The best-resolved quantities are the strike and depth of dipping fabric contrasts or interfaces. We find a strong geographic gradient in such anomalies, with large amplitudes extending inboard from the present-day subduction margin, the Aleutian arc, and an influence of flat-slab subduction of the Yakutat microplate north of the Denali fault. An east–west band across interior Alaska shows low-amplitude crustal anomalies. Anomaly amplitudes correlate with structural intensity (density of aligned geological elements), but are the highest in areas of strong Cenozoic deformation, raising the question of an influence of current stress state. Imaged subsurface strikes show alignment with surface structures. We see concentric strikes around arc volcanoes implying dipping magmatic structures and fabric into the middle crust. Regions with present-day weaker deformation show lower anomaly amplitudes but structurally aligned strikes, suggesting pre-Cenozoic fabrics may have been overprinted or otherwise modified. We observe general coherence of the signal across the brittle-plastic transition. Imaged crustal fabrics are aligned with major faults and shear zones, whereas intrafault blocks show imaged strikes both parallel to and at high angles to major block-bounding faults. High-angle strikes are subparallel to neotectonic deformation, seismicity, fault lineaments, and prominent metallogenic belts, possibly due to overprinting and/or co-evolution with fault-parallel fabrics. We suggest that the underlying tectonic grain in the northern Cordillera is broadly distributed rather than strongly localized. Receiver functions thus reveal key information about the nature and continuity of tectonic fabrics at depth and can provide unique insights into the deformation history and distribution of regional strain in complex orogenic belts.

Cite this article as Schulte-Pelkum, V., J. S. Caine, J. V. Jones, III, and T. W. Becker (2020). Imaging the Tectonic Grain of the Northern Cordillera Orogen Using Transportable Array Receiver Functions, *Seismol. Res. Lett.* **XX**, 1–20, doi: 10.1785/0220200182.

Supplemental Material

Introduction

Primary questions we seek to address with this study are how strain is distributed laterally and with depth through the crust over time, and whether structural inheritance and reactivation play a role in controlling present-day deformation. We investigate the extent to which these questions can be addressed by seismic imaging of the tectonic grain of the northern Cordillera orogen (NCO). We define tectonic grain as the 3D preferential orientation of geologic features and their topographic and geomorphologic expressions of fault and shear zones, veins, folds, unit contacts, pluton elongations, foliations, and lineations that developed and evolved in response to a regional-scale, coherent stress-strain field.

We introduce a broad overview for the tectonic and geologic framework in the remainder of this section. In the following sections, we describe the seismic dataset, processing, azimuthal receiver function analysis, and results. Results are put into context with topography, geology, and tectonics in the discussion and conclusions by examining the correlations of seismically imaged fabrics at depth with structural features.

1. Cooperative Institute for Research in Environmental Sciences and Department of Geological Sciences, University of Colorado, Boulder, Colorado, U.S.A.; 2. U.S. Geological Survey, Denver, Colorado, U.S.A.; 3. U.S. Geological Survey, Anchorage, Alaska, U.S.A.; 4. Department of Geological Sciences and Institute for Geophysics, Jackson School of Geosciences, The University of Texas at Austin, Austin, Texas, U.S.A.

*Corresponding author: vera.schulte-pelkum@colorado.edu

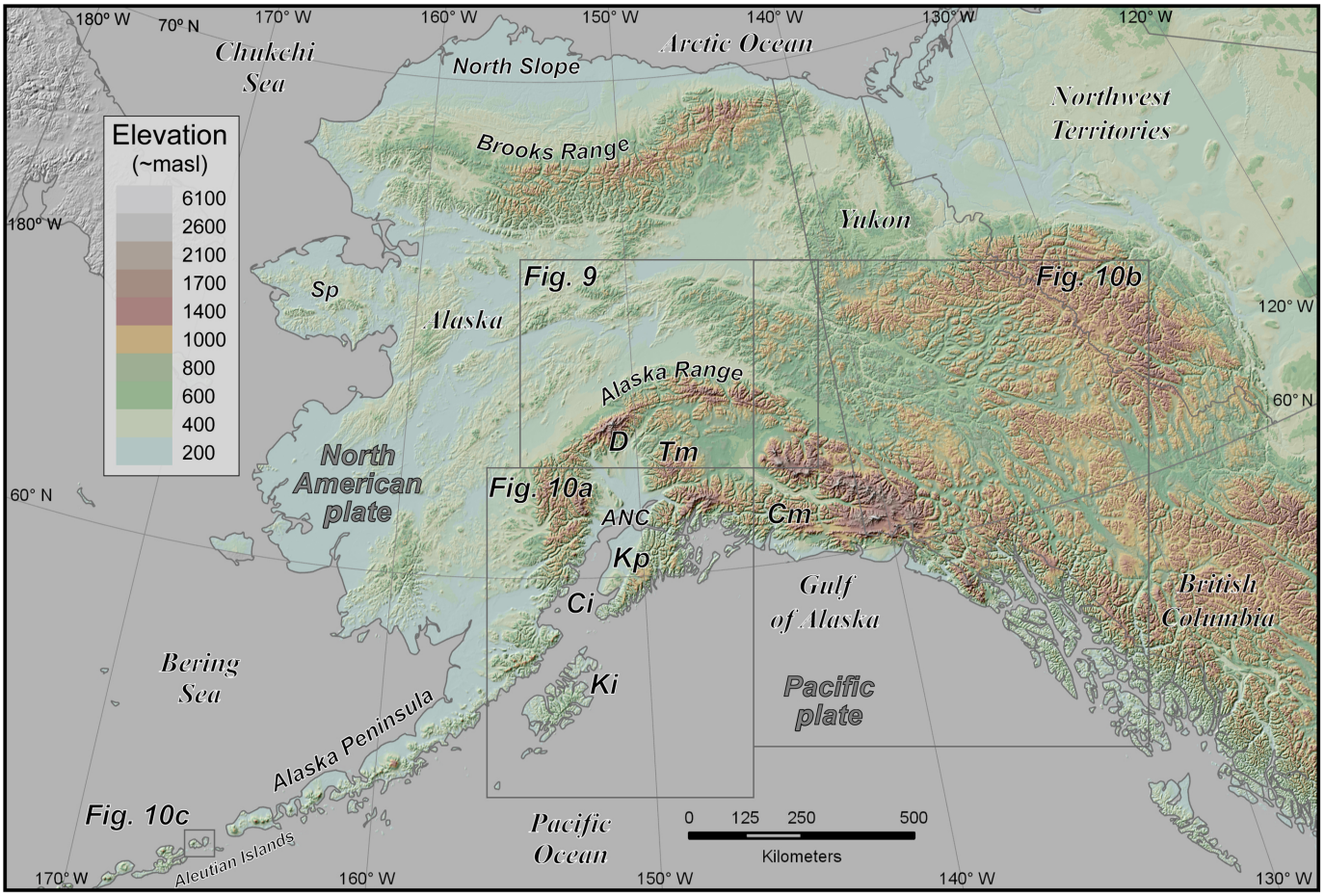

Figure 1. Study area with major geographic elements in Alaska, Yukon, and parts of the Northwest Territories and British Columbia (GTOPO 30 m DEM, 2020; Approximate meters above sea level [~masl] are shown for reference). Boxes show outlines of larger-scale maps in Figures 9 and 10. ANC, Anchorage; Ci, Cook Inlet; Cm, Chugach Mountains including the Chugach–St. Elias fold and thrust belt; D, Denali (mountain); Ki, Kodiak Island; Kp, Kenai Peninsula; Sp, Seward Peninsula; Tm, Talkeetna Mountains. The color version of this figure is available only in the electronic edition.

Tectonic and Geologic Framework

The NCO (Fig. 1) of Alaska, Yukon, and British Columbia is a region characterized by the complexly modified margin of ancestral North America or Laurentia, surrounded by a collage of accreted continental and oceanic terranes (Fig. 2; Coney *et al.*, 1980; Colpron *et al.*, 2007; Monger and Daniel Gibson, 2018). The vast majority of terranes that make up the NCO formed and evolved outboard of North America prior to accretion, and many have geologic origins and tectonic affinities that are different from adjacent terranes. Some have shared deformational histories prior to final accretion and integration into the NCO, whereas others have more unique histories. This complex history makes it difficult to unravel the tectonic events through which the orogen evolved from surface data alone. Adding to the challenge, the NCO spans a vast and remote region, making large-scale geophysical data important to building a refined understanding of the regional tectonic framework (for example Pavlis *et al.*, 2019).

The geology of the region reflects hemispheric interactions among the North American, Eurasian, and Panthalassic–Pacific plates, microplates such as Arctic Alaska–Chukotka and Yakutat (Fig. 2), and numerous tectonic fragments with a range of composition, structure, and affinity (Grantz *et al.*, 1994; Plafker and Berg, 1994; Colpron and Nelson, 2009; Pease and Coakley, 2018, and references therein). Plate interactions from the late Proterozoic through the present day are recorded by punctuated or prolonged events that include (1) terrane accretion, translation, and modification; (2) formation and closure of fringing ocean basins and intracontinental basins; (3) burial, regional metamorphism, and exhumation of large regions; (4) formation of regional fold and thrust belts; (5) growth, evolution, and demise of magmatic arcs; and (6) formation of crustal-scale plastic-to-brittle structural zones that accommodate hundreds to thousands of kilometers of displacement (Moore *et al.*, 1994; Plafker and Berg, 1994; Dusel-Bacon *et al.*, 2006; Gabrielse *et al.*, 2006; Bradley *et al.*, 2014; Moore and Box, 2016; Trop *et al.*, 2019). The NCO primarily is

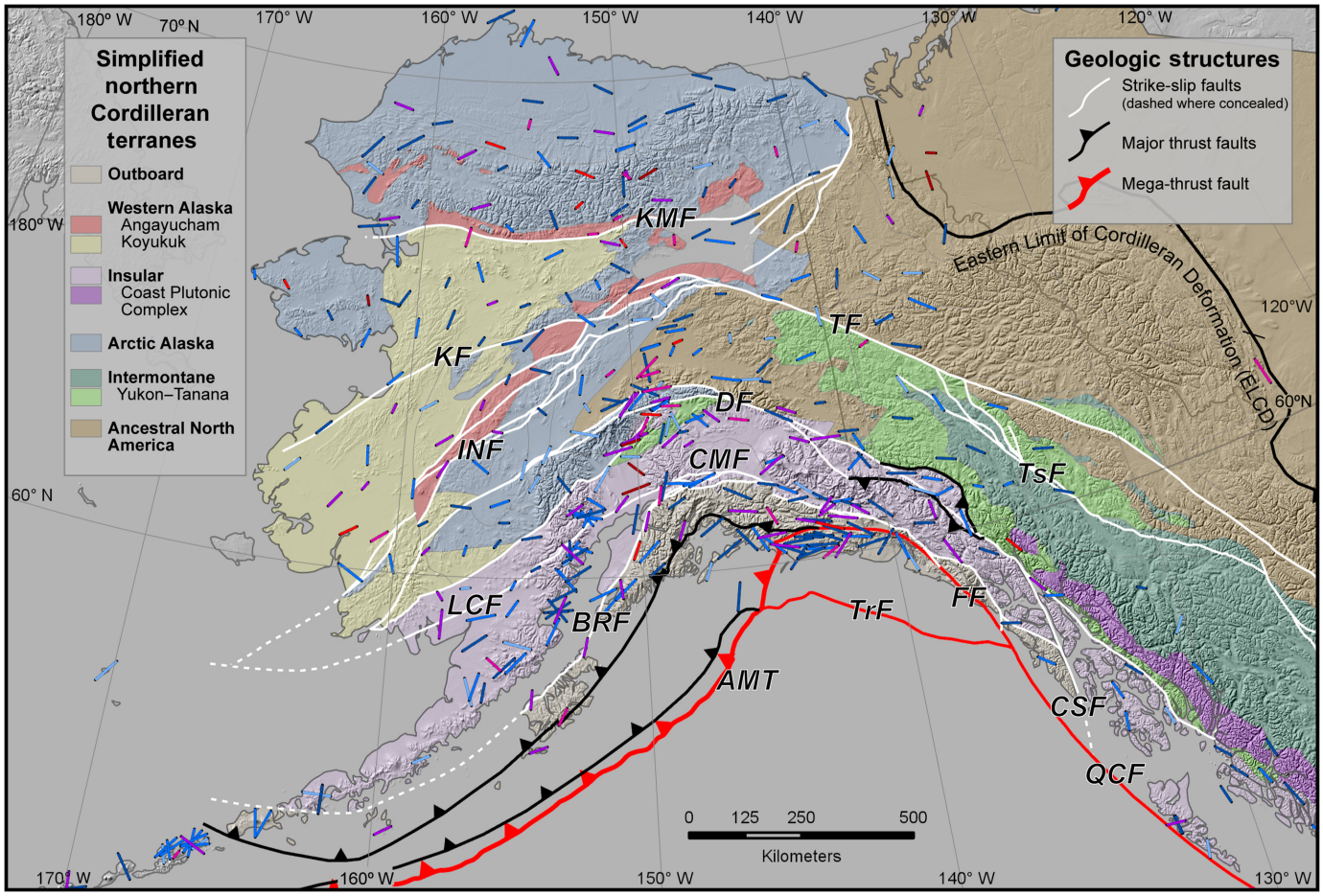

Figure 2. Major terranes grouped by tectonic affinity overlaid on digital elevation model (DEM; modified from Colpron and Nelson, 2011). Major faults include AMT, Aleutian megathrust; BRF, Border Ranges; CMF, Castle Mountain; CS, Chatham Strait; DF, Denali; INF, Iditarod–Nixon Fork; ELCD, eastern limit of Cordilleran deformation (modified from Colpron and Nelson, 2011); FF, Fairweather; LCF, Lake Clark; KF, Kaltag; KMF, Kobuk–Malamute; QCF, Queen Charlotte; TF, Tintina; TrF, Transition; TsF, Teslin. Bars show strike (orientation), depth (fill), and amplitude of maximum amplitude A1-harmonic receiver function arrival (interpreted as foliation strike at depth), described in more detail in the Analysis for Plunging Axis Anisotropy and Interface Dip section (scales as in Fig. 6). The color version of this figure is available only in the electronic edition.

a contractional orogen, but it also records extension in multiple regions and significant oblique convergence that produced interacting sets of long, transcurrent shear zones and faults with large displacements (Fig. 2; Reed and Lanphere, 1974; Eisbacher, 1985; Miller and Hudson, 1991; Pavlis *et al.*, 1993; Miller *et al.*, 2002; Pavlis and Roeske, 2007; Bemis *et al.*, 2015; Murphy, 2018).

Orogen-scale fabrics can include features such as dipping contacts, regional-scale foliations, and zones of localized plastic strain in basement rock assemblages. Such contrasts are mappable across the NCO using teleseismic receiver functions (Schulte-Pelkum and Mahan, 2014a,b; Schulte-Pelkum *et al.*, 2020). Seismic velocity or anisotropy contrasts, as identified through this method, may represent contrasts that are formed by (1) crystalline basement or batholith contacts with sedimentary basins or other intrusive contacts, (2) contacts between sedimentary lithologies with sufficient contrast, (3) regional folds and fault zones in which contrasting units are juxtaposed, and (4) shear zones. Although numerous near-surface topographic, geologic, and tectonic features make up an overall tectonic grain in the NCO, the depth to which surface structures are related to features at depth is poorly understood.

Plafker and Berg (1994, and references therein) and, more recently, Colpron *et al.*, (2007) and Nelson *et al.* (2013) provide a lithotectonic framework that is useful for interpreting the orogen-scale geophysical observations for the northern Cordillera (Fig. 2). Figure 2 shows a simplified grouping of major terranes. The NCO has a distinctive, arcuate geometry centrally transected by an oroclinal hinge that originates in the indenter corner of the eastern Aleutian megathrust in the Gulf of Alaska and trends north through a series of major strike-slip faults within the plate (Fig. 2; compare with Plafker and Berg, 1994; Glen, 2004; Eberhart-Phillips *et al.*, 2006; Murphy, 2018).

The orogen is cored by the northwestern margin of ancestral North America (ANA, also known as cratonic Laurentia, Fig. 2), which comprises thick Proterozoic and Paleozoic carbonate and siliciclastic successions deposited along the ancient continental margin. The sedimentary packages are estimated to be a few kilometers to more than 10 km thick and are underlain by crystalline basement rocks (e.g., Moore *et al.*, 1994; Strauss *et al.*, 2013). ANA is bounded on the north by Arctic Alaska terranes (AAT) that extend to the west across northern Alaska, encompassing the Brooks Range, North Slope, and Seward Peninsula of Alaska (Figs. 1 and 2; Moore *et al.*, 1994; Amato *et al.*, 2009; Grantz *et al.*, 2011; Till, 2016; Miller *et al.*, 2018). The AAT is a continental terrane with northern Laurentian, Baltic, and Siberian origins (e.g., Strauss *et al.*, 2013) that forms a tectonic block with distinctive seismotectonic fabrics compared with ANA. Accretionary or translational components of AAT along the northern ANA margin initially formed in the Paleozoic and culminated in the Mesozoic during a major collisional event that formed the Brooks Range orogen (Till, 2016).

The southern part of the ANA margin was displaced hundreds of kilometers to the west by the Tintina fault (Gabrielse *et al.*, 2006), and a large region of eastern interior Alaska is underlain by structurally modified ANA strata and associated crystalline basement (Fig. 2; e.g., Templeman-Kluit, 1976). These ANA assemblages are generally in low-angle thrust, or extensional contact with accreted terranes that surround them. Ancient, margin-parallel, polyphase extensional and overprinting, polyphase contractional fabrics in the basement rocks of ANA likely form regional-scale contrasts that form the deep-seated seismotectonic grain and influence seismic anisotropy in the central interior portion of the orogen. The southern ANA margin is bounded by a diverse suite of largely continental lithotectonic assemblages that make up the Intermontane terranes (Fig. 2; Templeman-Kluit, 1976; Pavlis *et al.*, 1993; Dusel-Bacon *et al.*, 2006; Colpron *et al.*, 2007). The Intermontane terranes, typified in eastern Alaska by the Yukon–Tanana terrane (YTT, Fig. 2), form a belt of siliciclastic continental margin strata intruded by quartzofeldspathic batholiths that were structurally buried, regionally metamorphosed, and exhumed in the Mesozoic. These characteristic components of the Intermontane terranes also likely have regional-scale grain that influences seismic observations. Most of the Intermontane terranes (Fig. 2) are cored not only by the same geology with similar bulk composition as ANA, but they also contain rocks with more phyllosilicates and carbonates that are complexly infolded and faulted together with their quartzofeldspathic crystalline basement. To the south, the Intermontane terranes are bounded by the Denali fault that hosts up to ~400 km of dextral displacement, and, together, the Tintina and Denali faults (Figs. 2 and 3) have accommodated oblique convergence inboard of the North American–Pacific plate margin since the late Mesozoic (e.g., Eisbacher, 1976; Gabrielse *et al.*, 2006). The YTT and ANA are also transected by multiple northeast-striking aeromagnetic lineaments interpreted to represent Mesozoic or Cenozoic fault zones (Fig. 2; Sánchez *et al.*, 2014). In some places, these enigmatic lineaments are mapped as faults and are collocated with zones of spatially distributed modern and historical seismicity. Some lineaments also coincide, to some degree, with known mineral deposits (northern subareas outlined in Fig. 1; Page *et al.*, 1995; Allan *et al.*, 2013; Tape *et al.*, 2015).

The Denali fault also marks the contact between the inboard, Intermontane terranes and the outboard, exotic Insular terranes to the south (Fig. 2). The Insular terranes form a belt that is made up of three exotic subterranes—Wrangellia, Alexander, and Peninsular—that formed outboard of ANA and that were accreted in the Mesozoic. These terranes include extensive Paleozoic through Cenozoic nonarc and arc mafic volcanic rocks, magmatic arc rocks, greenstone belts, oceanic plateau rocks, interrelated volcanogenic back-arc, and fore-arc basin rocks (Fig. 3; Plafker and Berg, 1994; Colpron *et al.*, 2007; Beranek *et al.*, 2014). Assemblages with significant components of mafic rocks juxtaposed with more felsic rock assemblages could be a source of fabric contrast that may contribute substantially to the overall tectonic grain. Parts of the Insular belt are overlapped by a Mesozoic–Cenozoic fore-arc basin that contains up to 18 km of siliciclastic sediment (Cook Inlet, Fig. 1; Lepain *et al.*, 2013; Feng and Ritzwoller, 2019a). The Intermontane and Insular terranes are intruded by multiple and geographically extensive belts of Mesozoic and Cenozoic magmatism that are approximately parallel to the southern Alaska margin (Fig. 3). These magmatic belts extend into the NCO across the Denali and Tintina faults, and some contain a variety of ore deposits thought to reflect deeper crustal fabrics that may have influenced their localization and emplacement (e.g., Plafker and Berg, 1994; Mair *et al.*, 2011; Allan *et al.*, 2013; Regan *et al.*, 2020). In addition to the Denali fault, the Insular terranes are bounded or also cross cut by other major, seismically active, crustal-scale faults that include the Chatham Strait, Lake Clark, Castle Mountain, Border Ranges, and Queen Charlotte faults (Figs. 2 and 3; Plafker and Berg, 1994; Colpron *et al.*, 2007).

Western Alaska (late accreted) terranes (WAT) surround the western and southernmost margins of the orogen (Fig. 2; Plafker and Berg, 1994; Colpron *et al.*, 2007). These terranes are largely exotic to ANA and have unique, disparate geologic histories and tectonic grain. Some are of continental affinity (e.g., Bradley *et al.*, 2014), such as the Farewell and Koyukuk terranes, whereas others such as the Angayucham terrane are oceanic (Fig. 2; Barker *et al.*, 1988). A large region of western Alaska is underlain by Mesozoic marine volcanic arc rocks and >8 km of volcanogenic and clastic accretionary sedimentary rocks of the Koyukuk terrane that are broadly folded and thrusted (e.g., Patton, 1973; O'Brien *et al.*, 2018). Large orogen-parallel bodies to small klippen of complexly obducted

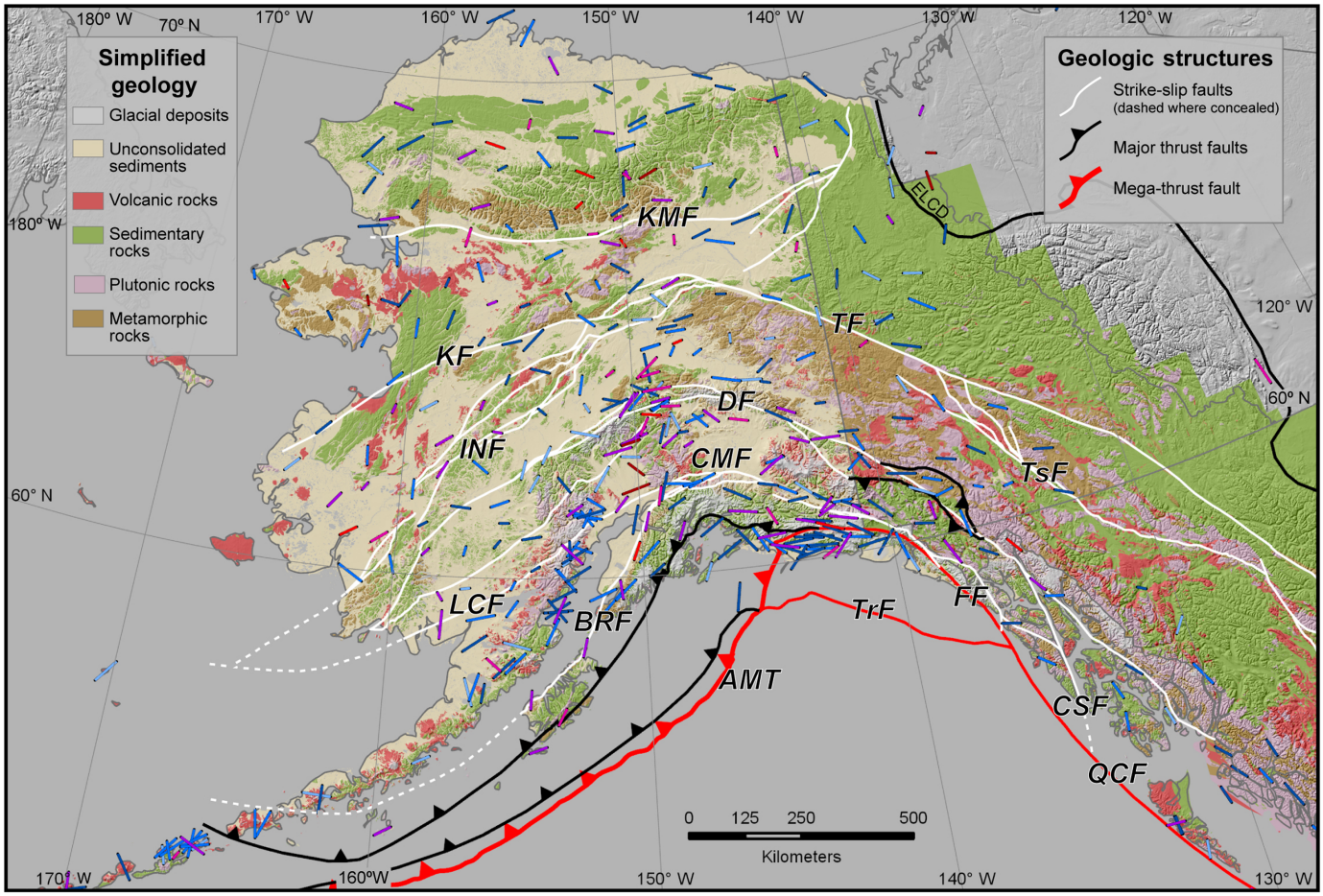

Figure 3. Surface and bedrock geology overlaid on DEM (modified from Colpron and Nelson, 2011; Wilson *et al.*, 2015; Cui *et al.*, 2017; Yukon Geological Survey, 2020), else as in Figure 2. The color version of this figure is available only in the electronic edition.

ophiolite assemblages form the northeastern margin of the WAT in which it is in contact with the AAT, ANA, and YTT (Fig. 2; Colpron *et al.*, 2007).

The Chugach accretionary complex and Yakutat microplate make up the outboard terranes (OTs; south of Insular terranes in Fig. 2) and form the southern margin of the NCO. The Chugach complex comprises heterogeneous sedimentary rocks deposited in the Mesozoic–Cenozoic ocean trench along the southern Alaska and western North American margin (Plafker, 1987). The Yakutat block is a 15–35 km thick oceanic plateau that formed in the late Paleogene and began subducting beneath southern Alaska in the Oligocene. The shallow dip of the thick, subducted Yakutat crust produced a gap in arc magmatism across south-central Alaska that persists to the present. The 3D geometry of the Yakutat block has been imaged seismically (Eberhart-Phillips *et al.*, 2006, and references therein; Feng and Ritzwoller, 2019a; Berg *et al.*, 2020) and shows a complex, slab-related crustal signature, crustal thickening, and surface uplift well north of the Denali fault through the oroclinal hinge (Eberhart-Phillips *et al.*, 2006; Benowitz *et al.*, 2011). Major faults bounding the OTs include the Border Ranges fault system, a tens of kilometers wide zone of complex, distributed deformation (Fig. 2 and western detailed view outlined in Fig. 1; Pavlis and Roeske, 2007). The offshore Transition and Queen Charlotte faults intersect in the indenter corner in which contractional and strike-slip deformation is highly partitioned (Fig. 2; Koons *et al.*, 2010).

The Aleutian volcanomagmatic arc extends thousands of kilometers from south-central Alaska through the Alaska Peninsula and Aleutian Islands to the west (Fig. 1). The Aleutian arc initiated in the Eocene and is presently active (e.g., Vallier *et al.*, 1994; Jicha *et al.*, 2006). It is built on the preexisting crust of the Insular belt in south-central Alaska and the Alaska Peninsula, but it becomes an intraoceanic arc to the west, where it separates the Pacific plate from the Bering basin to the north. Modern plate convergence vectors are at high angles to the trend of the Alaska Peninsula segment of the modern arc (DeMets *et al.*, 2010; see also Fig. S1, available in the supplemental material to this article), and they are almost parallel to the trend of the arc at its western end.

Data and Methods

Data

We used data acquired from the EarthScope Alaska Transportable Array (network code TA) from May 2014 through January 2020, including some stations of the Alaska Volcano Observatory. We added permanent broadband stations from the Alaska Regional Network for 2014 through January 2020 and Canadian National Seismic Network from 2010 through January 2020, augmented with data from two temporary broadband deployments—Broadband Experiment Across the Alaska Range (1999–2001; Christensen *et al.*, 1999) and Observational and Theoretical Constraints on the Structure and Rotation of the Inner Core (2004–2007; Song and Christensen, 2004).

Within those timeframes, all teleseismic events of magnitude 5.0 and greater with event-station epicentral distances of 28°–150° were retrieved for time windows of 2 min surrounding the *P* or P_{diff} arrival. Data were obtained and preprocessed from the Incorporated Research Institutions for Seismology's Data Management Center using Standing Order for Data (Owens *et al.*, 2004).

Processing

Ps radial- and transverse-component receiver functions were calculated for all events using a time-domain iterative deconvolution method (Ligorria and Ammon, 1999, with modifications according to Wilson *et al.*, 2003, and Schulte-Pelkum and Mahan, 2014a). The deconvolution yields absolute amplitude receiver functions in units of horizontal-to-vertical-component amplitude ratio. We chose a Gaussian filter factor of 3 (Ligorria and Ammon, 1999), corresponding to a pulse length of slightly less than 1 s, which allows resolution within the crust while suppressing noise. Quality control was performed automatically using criteria for signal-to-noise ratio, variance reduction, maximum amplitude, characteristics of the direct radial *P* pulse, and pulse length, as described in detail in Schulte-Pelkum and Mahan (2014a). We processed nearly five million initial receiver functions from 38,534 events and 486 stations. The harmonic analysis requires azimuthal gaps of less than 90° at each station. After automated quality control of each receiver function and discarding stations with azimuthal gaps, we retained 437,204 receiver functions at 477 stations for analysis.

Analysis for plunging axis anisotropy and interface dip

Contrasts in *P* anisotropy with a plunging symmetry axis on at least one side of an interface lead to receiver function arrivals that change polarity with back azimuth (one positive and one negative peak across all back azimuths; first azimuthal harmonic, here denoted as A1). Schulte-Pelkum and Mahan (2014a,b) introduced a method that combines these signals on both radial and transverse components in receiver functions. Because the positions of the A1 amplitude minimum, maximum, and polarity nodes show a 90° phase shift in back azimuth between radial and transverse components (Schulte-Pelkum and Mahan 2014a,b), the method is particularly useful at temporary stations that may otherwise have azimuthal gaps (compare with Rasendra *et al.*, 2014, who use a subset of stations also in our study for anisotropic receiver function analysis but state that a lack of azimuthal coverage prevents them from characterizing the anisotropy). Receiver functions are inherently more sensitive to plunging axis anisotropy than to purely azimuthal anisotropy (Levin and Park, 1998; Schulte-Pelkum and Mahan, 2014a; Park and Levin, 2016), and we focus on the former geometry.

The method resolves the depth of a contrast via its delay time (*S-P* time, scaled to depth via *P* and *S* velocity above the converter as in standard receiver function analysis). In addition, the polarity change of an arrival occurs at the strike of the plane perpendicular to the symmetry axis in the anisotropic case (Schulte-Pelkum and Mahan, 2014a,b). This plane corresponds to a foliation plane for most crustal rocks in which the anisotropy is dominated by phyllosilicate-rich lithologies (e.g., biotite), which form hexagonal slow-axis symmetry with a fast foliation plane (Brownlee *et al.*, 2017). Amphibole-rich rocks are also the best approximated by slow-axis symmetry, although they can sometimes form fast-axis symmetry depending on deformation conditions (Ji *et al.*, 2013; Brownlee *et al.*, 2017). In the lower crust, plagioclase can align with its fast axis perpendicular to foliation (Bernard and Behr, 2017), so our method again would return foliation strike. Unlike splitting, our method is not path cumulative, and a contrast in anisotropy of a few percent over a scale of 2–3 km is sufficient to generate a robustly observable signal (Schulte-Pelkum and Mahan, 2014a).

Dipping contrasts between isotropic layers also generate A1-harmonic signals (Jones and Phinney, 1998; Savage, 1998). In this case, polarity reversals also occur at the strike of the dipping contrast. Although a distinction between dipping isotropic layers versus subsurface plunging axis anisotropy can be made by analyzing the direct *P* arrival (Schulte-Pelkum and Mahan, 2014a), we analyze both cases in this contribution as an expression of large-scale tectonic grain; dipping contacts likely have similar strikes to foliation contrasts associated with solid-state deformation fabrics (Schulte-Pelkum *et al.*, 2020).

The amplitude of an A1 arrival depends not only on the magnitude of the contrast across an interface, but also on the angle of foliation or interface dip (Schulte-Pelkum and Mahan, 2014a,b). The signal from a given contrast in anisotropy is maximized for intermediate dip angles of foliation (Schulte-Pelkum and Mahan, 2014a; Brownlee *et al.*, 2017). End members include radial anisotropy (horizontal foliation with hexagonal symmetry), when the signal would mimic a flat contrast between isotropic layers (A0—no azimuthal dependence; Schulte-Pelkum and Mahan, 2014b), and purely

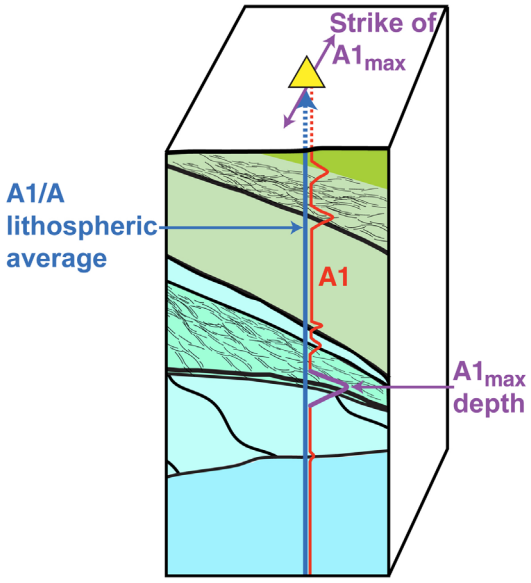

Figure 4. Illustration of the quantities displayed in A1/A and $A1_{max}$ maps. The triangle is a seismic station on top of the lithosphere in which dipping boundaries and rock deformation fabrics occur. The harmonic analysis yields A1 amplitudes as a function of delay time and therefore depth (wiggly line). A1 amplitude from harmonic decomposition as well as total absolute receiver function amplitude A normalized by number of events can be averaged over all lithospheric depths (vertical arrow). We display the percentage of the A1-harmonic signal with respect to the total absolute receiver function amplitude (Fig. 5). For the largest amplitude A1 arrival (largest peak) at each station, we plot its depth ($A1_{max}$ depth). This arrival has an associated phase at 90° to the strike of dipping foliation at the converting contrast or the strike of the dipping interface separating two layers. We plot this strike and the depth of the converter at the station location (arrow) in Figures 1–3 and 6. The color version of this figure is available only in the electronic edition.

azimuthal anisotropy (vertical foliation with hexagonal symmetry), when the signal becomes A2 (second azimuthal harmonic; Levin and Park, 1998). Actual rock-based tensors result in A1 and A2 components even for vertical or horizontal foliation (Schulte-Pelkum and Mahan, 2014b; Brownlee *et al.*, 2017).

Results

We present the results of the resolved A1-harmonic signal in two forms—depth-averaged amplitude and peak arrival (Fig. 4). A1 signal amplitude can be averaged over a given length of the receiver function for a depth-averaged measure of the amplitude of the first harmonic compared to the total averaged receiver function amplitude. Figure 5 shows a map of A1 amplitude as a percentage of total receiver function amplitude, averaged from 0 to 15 s, a time range that encompasses the entire lithosphere (depth to ~150 km). The values are interpolated between stations using tension splines (Smith and Wessel, 1990), in which maximum and minimum values are constrained to occur at station locations. The values provide a measure of how much of the total receiver function signal may be explained by contrasts with dipping foliation or other dipping contrasts.

A1 amplitudes are highest along the Aleutian arc, in southern Alaska, from the coast to the central Denali region paralleling the subducting Pacific slab and in the area of Yakutat flat-slab subduction. The interior surrounding the Tintina and Kaltag faults to the Seward Peninsula shows low amplitudes. The lithosphere-integrated A1 amplitude is elevated again in the vicinity of the Brooks Range and along parts of the northern coast.

We next show the amplitude, depth (from delay time), and strike of the largest amplitude A1 arrival at each station (Fig. 6a), as well as its amplitude uncertainty (Fig. 6b). Whereas each station has multiple peaks in the A1-harmonic solution at different times (Fig. 4), corresponding to conversions from different depths, the maximum A1 amplitude solution at each station is presumed to be its best constrained arrival (Schulte-Pelkum *et al.*, 2020). As discussed in the Analysis for Plunging Axis Anisotropy and Interface Dip section and in previous publications (Schulte-Pelkum and Mahan, 2014a,b; Brownlee *et al.*, 2017), we interpret the strike of those maximum A1 peaks as strikes of contrasts in crustal foliation or strikes of dipping boundaries between relatively isotropic bodies. They should, therefore, be comparable to mapped foliations integral to the regional tectonic grain and alignment of geological units with significant contrasts. We exclude peaks at zero delay time, because they represent A1 periodicity in a bent *P* wave rather than the converted *S* wave.

We show the station-maximum A1 arrivals ($A1_{max}$) in Figure 6. In Figure 6a, the maximum arrival is represented as a line with length binned by A1-arrival amplitude, orientation representing the strike of foliation or dipping interface, and line fill color representing the depth of the arrival. We also calculate the uncertainty of the A1-arrival amplitude by employing a bootstrap error method that solves for A1 amplitude and phase while omitting random azimuthal bins in 100 instances and calculates a 95% confidence interval based on the resulting distribution. Figure 6b shows the maximum A1 amplitude and strike at each station as three populations: one with A1 amplitude uncertainty from bootstrapping of less than 30% of the A1 amplitude, one with uncertainty of 30%–60% of the A1 amplitude, and one with uncertainty >60%. We display solutions with uncertainties of less than 60% in all other maps. The depth distribution for the set with amplitude uncertainty ≤60% is shown in Figure 7a, a representative north–south swath within the set and with amplitude uncertainty ≤30% are shown as a function of latitude in Figure 7a, and orientation comparisons to structural features for the set with amplitude uncertainty ≤60% are plotted in Figure 8. Subregions of Figure 6a are shown in Figures 9 and 10.

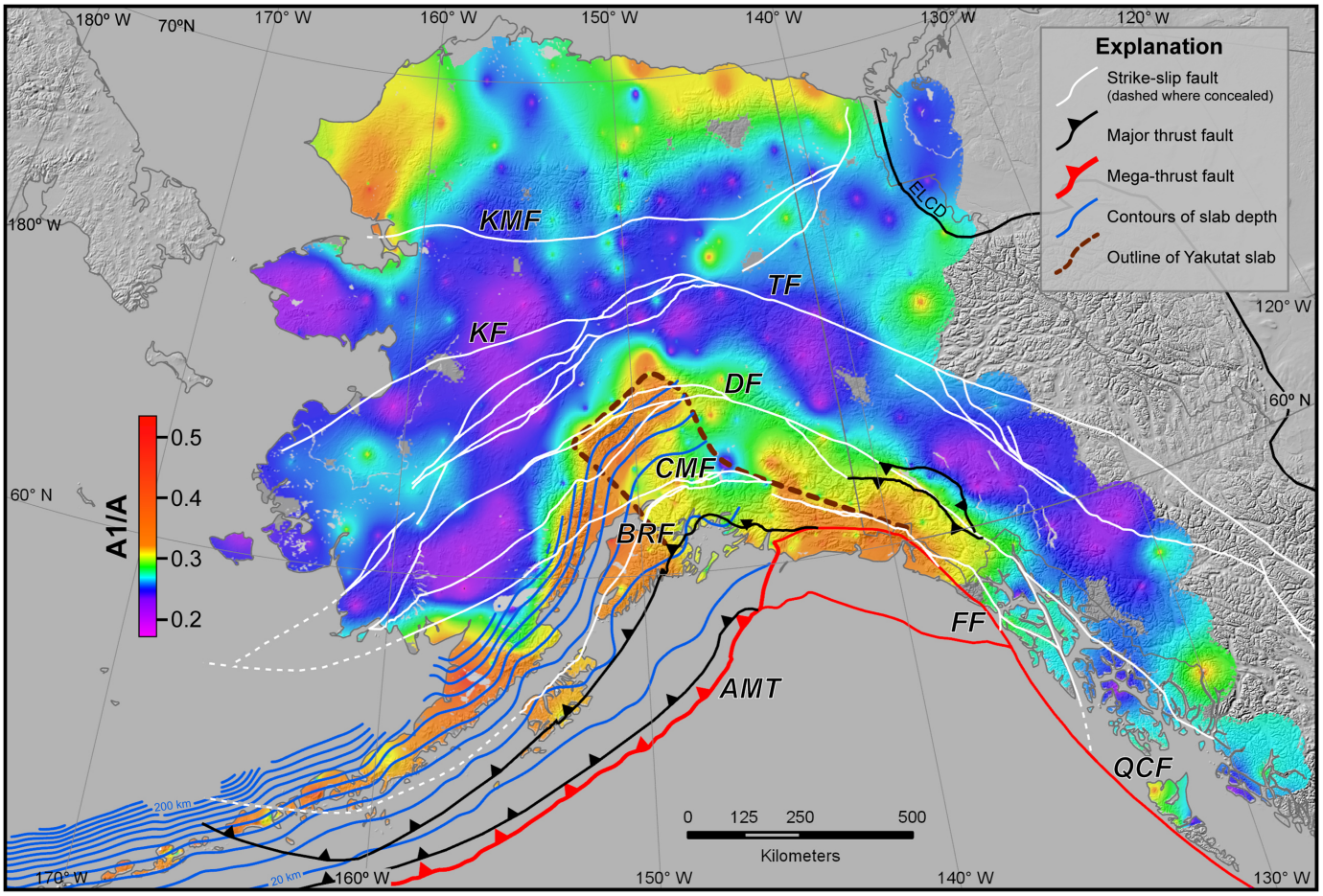

Figure 5. Receiver function amplitude in the first azimuthal harmonic (A1) as a fraction of the total receiver function amplitude for all stations, averaged over all lithospheric depths. A value of A1/A of 0.5 means that 50% of the amplitude in the receiver functions is found in the first azimuthal harmonic. Dark areas have small deformation/dip signal integrated through the lithosphere and light areas show larger deformation/dip signal. A1/A is draped on DEM showing major faults as in Figure 2, contours of Pacific plate slab (Hayes *et al.*, 2012; 20 km contour intervals, starting at 20 km depth increasing northeastward to 200 km) and the outline of the Yakutat slab (dashed brown, modified from Eberhart-Phillips *et al.*, 2006). The color version of this figure is available only in the electronic edition.

Between the maximum A1-arrival amplitude in Figure 6 and the lithosphere-averaged A1 amplitude in Figure 5 is a clear but nonuniform correspondence; some stations may register a large A1 contrast at one depth yet have a relatively low depth-averaged A1 amplitude. The maximum arrival amplitude pattern is again one of larger A1 from the arc and plate boundary to the vicinity of the central Denali fault, lower amplitudes in the interior but with local large arrivals, and slightly elevated amplitudes in the Brooks Range and northern coastal region.

Despite significant variability in the strikes, there are local and regional systematic trends on length scales are typically not accessible to such receiver function analysis. Unique radial to fan-shaped scatter at very closely located stations is seen around volcanic edifices on the Aleutian Islands and on the western side of the Cook Inlet along the Aleutian magmatic arc, for example. In a close-up view, the scatter resolves into circular arrangements of strikes surrounding the volcanic edifice in each case. An example for Akutan Volcano in the Aleutian arc is shown in the inset in Figure 10c. These arrivals also tend to be from the middle crust.

We interpret these concentric strike patterns as dipping volcanomagmatic fabric with concentric strikes, likely reflecting magmatic crystallization of intrusive bodies with some form of concentric geometry. Strong azimuthal effects in receiver functions were previously reported by Janiszewski *et al.* (2013, 2020) at Aleutian volcanoes and interpreted as the influence of low velocities in mid-crustal magma storage systems. However, their results suggest the possibility that strong arrivals with polarity reversals over back azimuth might have been misinterpreted as apparent azimuthal Moho arrival-time differences. A detailed analysis of the volcano signal we observe is beyond the scope of this article, but we propose that the signal derived from tangential as well as radial receiver functions

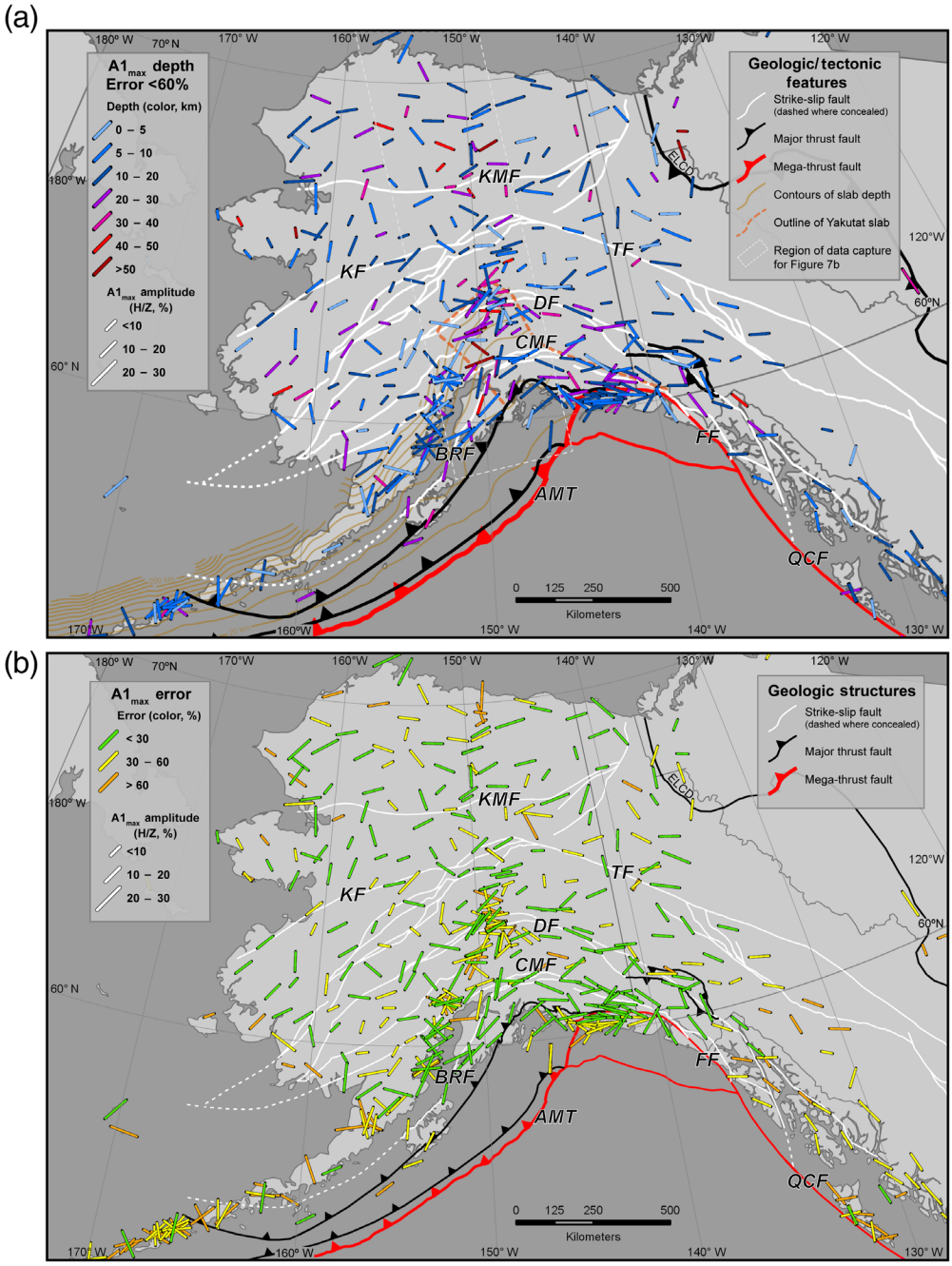

Figure 6. (a) Bars are the largest A1 arrival at each station where uncertainty is less or equal to 60% of the A1-arrival amplitude. Bar fill is depth, length is binned by amplitude of the arrival, and orientation of the bar corresponds to the strike of the foliation at a contrast or to the strike of a dipping interface. Starburst patterns are collocated with volcanoes and resolve into concentric circles (Fig. 10c). The dashed inset box shows the region of data captured and plotted in Figure 7b. (b) Station maximum arrivals and their strikes as in A, but fill here shows amplitude uncertainty from bootstrapping. Fault names are provided in Figure 2. H/Z, horizontal-to-vertical-component amplitude ratio. The color version of this figure is available only in the electronic edition.

in our analysis is more readily explained by dipping concentric fabrics or contrasts (Syracuse *et al.*, 2015), rather than a simple isotropic low-velocity conduit.

From the Gulf of Alaska north to the Denali and Tintina faults, receiver function strikes generally parallel the convergent plate boundary and the arcuate shape of the orogen as a whole. This area has the densest station coverage, and details are better seen in Figure 9. Going from east to west, receiver function-derived strikes are oriented northwest–southeast in southeastern Alaska, similar to the strike of the Queen Charlotte–Fairweather transform fault. They parallel east–west striking accretionary structures in the Border Ranges and Chugach–St. Elias fold and thrust belt (Fig. 10b), in which the structures and faults have been interpreted as recording transpressional deformation driven by long-lived oblique convergence (e.g., Plafker and Berg, 1994; Haeussler *et al.*, 2003; Bruhn *et al.*, 2012). Farther north, east-southeast–west-northwest strikes along the eastern Denali fault follow its central bend to more east–west strikes, then change to northeast–southwest along with the western Denali and Castle Mountain and Lake Clark faults (Figs. 6a, 9, and 10b).

On the Kenai Peninsula (Figs. 1 and 10a) and north past the Talkeetna Mountains (Figs. 1 and 6a), receiver function strikes are closer to north-northeast–south-southwest, paralleling the strikes of the Border Ranges fault and showing strikes similar to those of the depth contours of the Pacific slab. Immediately north of the apex of the Denali fault, receiver function strikes match those of the Northern Foothills fold and thrust belt (Fig. 9). The area between the Tintina and Denali faults east of 150° W is intersected by a series of northeast–southwest-striking

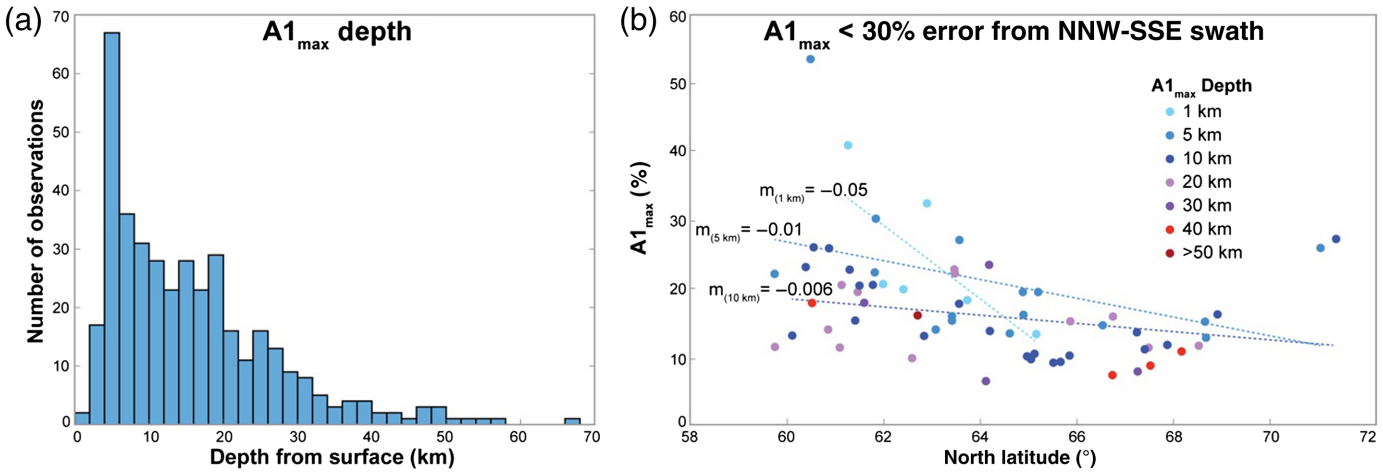

Figure 7. (a) Histogram of depth of largest A1 arrival ($A1_{max}$) observed at each station. (b) Scatter plot of largest A1 arrival ($A1_{max}$) observed at stations selected along a north-northwest–south-southeast (NNW-SSE) swath shown in Figure 6a. The gradients (m) of linear regressions of the 0–1, 1–5, and 5–10 km segregated data are also shown. The color version of this figure is available only in the electronic edition.

faults that merge southward into the Minto Flat and Fairbanks seismic zones (Tape *et al.*, 2015), and receiver functions in this area generally show similar northeast–southwest strikes.

In southwestern Alaska, the area between the Iditarod–Nixon Fork fault and the Kaltag fault (Figs. 1 and 2) shows dominant northeast–southwest receiver function strikes. Between the Kaltag fault and the Brooks Range, orientations are nearly north–south, but they are east–west across the Brooks Range and North Slope.

We converted delay times of the maximum A1 arrival ($A1_{max}$) at each station to approximate depths using a fixed average crustal *P* velocity (6.4 km/s) and *P* to *S* velocity ratio (1.73). Depths may vary by a few kilometers within the crust, because of deviations from assumed velocities above the converter; very deep values from the mantle may deviate by up to ~10 km or more. A histogram of $A1_{max}$ depths is shown in Figure 7a. Most $A1_{max}$ arrivals fall in the 4–20 km depth range. A peak at 4–6 km depth is followed by similar numbers of stations, with $A1_{max}$ falling between 6 and 20 km depth, then with a decrease of $A1_{max}$ depths beginning between 20 and 30 km depth and few arrivals below 50 km depth. Thus, most of the structures imaged by $A1_{max}$ in Figure 6a are in the seismogenic upper crust. More of the deeper arrivals are located in the vicinity of the Yakutat slab and near the Brooks Range, with most areas showing $A1_{max}$ arrivals spanning crustal depths. Values of the largest A1 arrival ($A1_{max}$) observed at stations are plotted along a north-northwest–south-southeast swath transecting the orogen parallel to the oroclinal hinge axis (Figs. 6a and 7b) and are binned by depth. Although the data are scattered, $A1_{max}$ appears to decrease south to north, particularly for values from shallower depths.

For quantitative comparisons of the degree of co-orientation and collocation between $A1_{max}$ strikes and structural elements, we plotted circular histograms of $A1_{max}$ strikes in Figure 8. Figure 8a shows all results with amplitude uncertainty of less than 60%. Figure 8b shows measurements within ~30 km on both sides of the Tintina–Kaltag faults. Figure 8c shows the same for the Denali fault as in Figure 8b and also shows orientations of the measured strikes with the average strikes of multiple fault strands (the parallel central Denali and Hines Creek fault segments are particularly densely sampled). $A1_{max}$ strikes within blocks bounded by faults (intrablock) co-oriented with northeast fault lineaments and seismicity, as well as with main fault traces, are shown in Figure 8d,e. Figure 8f,g shows intrablock data with poor co-orientation of fault-trace strikes north of the Kaltag fault to the Brooks Range (Kobuk–Malamute fault [KMF]) but strong co-orientation with the KMF for stations to the north.

Discussion

The observed receiver function fabrics from depth correlate with geological and topographic features at the surface and are interpreted to reflect orogen-scale tectonic grain. The strongest tectonic and deformational signal integrated through the lithosphere is focused in the south (Fig. 5), from the plate boundary to active subduction, oblique transform, and convergent structures. Geodetic velocities and earthquake moment tensors suggest strong components of transform motion along the Queen Charlotte–Fairweather fault in southeast Alaska (compare with Leonard *et al.*, 2007; Enkelmann *et al.*, 2015). However, our observation of high A1/A average amplitudes is more consistent with a dipping tectonic grain formed through long-lived transpression (Pavlis and Sisson, 2003), an interpretation that is also supported by the presence of young, high mountains in the area (e.g., Enkelmann *et al.*, 2008, 2009). We also attribute strong fabric contrasts that create the relatively large A1 arrivals from the Denali fault south to the plate margin to a combination of active subduction, oblique convergence, and faulting within the accretionary belts.

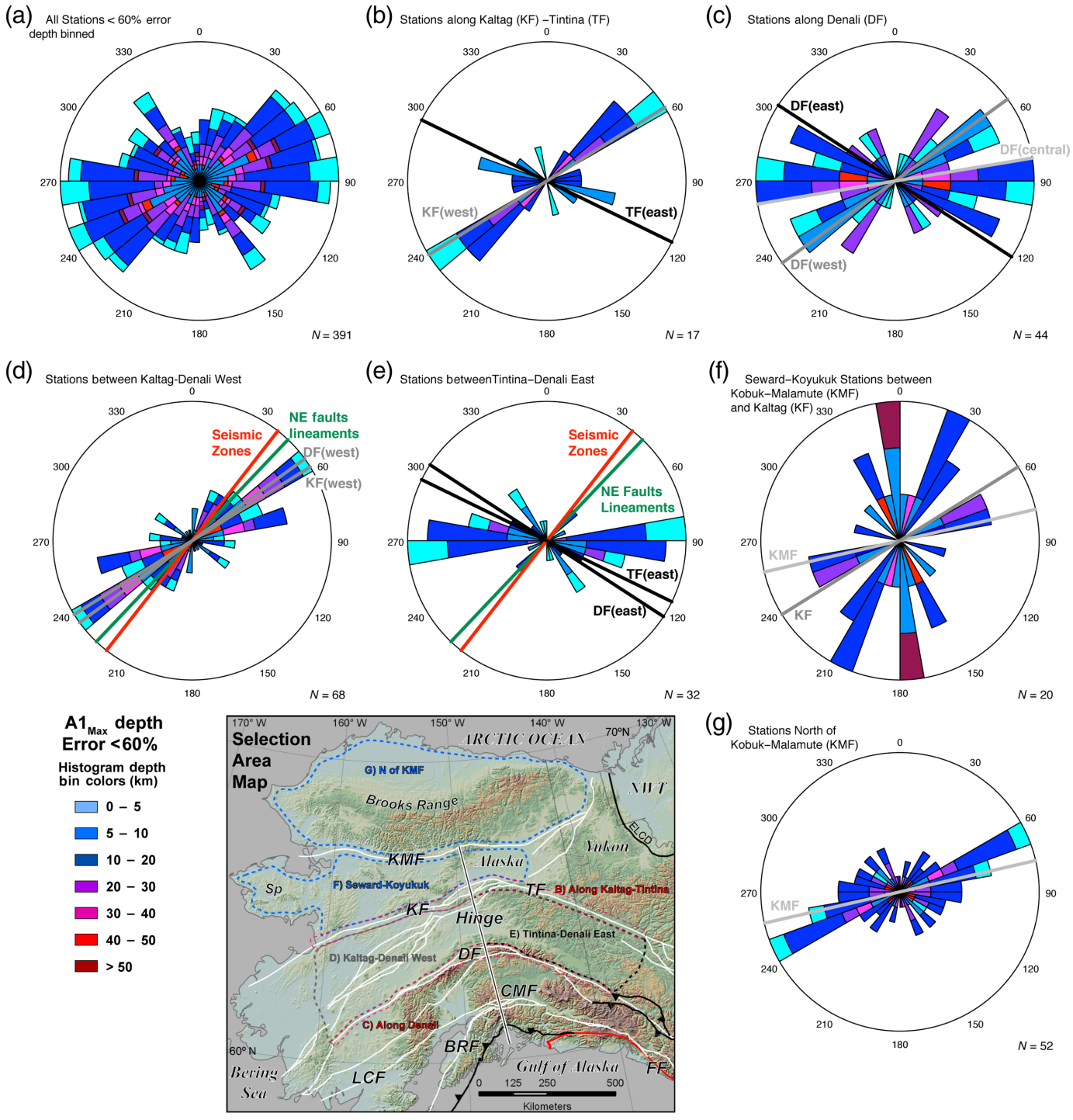

Figure 8. Equal distance, axial, circular histograms of $A1_{max}$ with major fault trends. (a) All stations with $A1_{max}$ uncertainty ≤60% binned by depth with fill scale, as in Figure 6a. (b–g) Select and representative groupings of stations with less than 60% $A1_{max}$ uncertainty, binned by depth. $A1_{max}$ strikes were selected within ~30 km on both sides of the traces along the faults indicated. The average strikes of major and minor faults, zones of seismicity, and lineaments are shown as individual lines (gray, western segments; black, eastern segments; light gray, west–east Denali central [and Hines Creek] segments; labeled, zones of seismicity and northeast faults and lineaments). Map shows topography and major faults, as in Figures 1 and 2, with selection areas corresponding to histograms of panels (b–g). The approximate location and orientation of the oroclinal hinge is also shown as a north-northwest-trending white and black line (compare with Murphy, 2018). The color version of this figure is available only in the electronic edition.

Although much of the central and eastern interior of Alaska consists of metamorphic rock with possible higher anisotropy (Brownlee *et al.*, 2017), low A1/A amplitudes surround the Teslin, Tintina, and Kaltag faults from western Yukon to the Seward Peninsula (Fig. 5). Most of the low-A1/A zones in the east-central Alaska (Fig. 5) coincide with ANA and the Intermontane terranes (Fig. 2), which are dominated by metamorphic and plutonic rocks exposed at the surface (Fig. 3). Maximum A1 arrivals in this area are from 20 km and shallower depths (Fig. 6a). These observations raise the possibility that metamorphic fabrics and fault zones mapped at the Earth's surface extend throughout and are representative of the structural character of the upper crust. Metamorphic fabrics are typified by open folds, shallowly dipping foliations, and low-angle shear zones that are consistent with lower A1 amplitudes compared to more steeply dipping foliations (Schulte-Pelkum and Mahan, 2014a,b; Brownlee *et al.*, 2017; Caine and Jones, 2020). Relatively undeformed plutonic rocks are also likely to have lower anisotropy than deformed metamorphic rocks (Christensen and Mooney, 1995). The upper- to mid-crustal $A1_{max}$ strikes that are imaged in this region are generally parallel to northeast-striking faults that are at a high angle to the southeast-striking Tintina fault. These observations may imply that fabric in the plastic lower crust and lithospheric mantle are not pronounced in this area, possibly due to overprinting or other age-related, fabric-altering processes active in the uppermost crust. The low-A1/A area near the Tintina fault partly overlaps with a prominent trend of late Mesozoic porphyry- and orogenic-style mineral deposits (e.g., Mortensen *et al.*, 2000).

West of the northern apex of the Denali and Tintina faults, a contrast between high A1/A amplitudes to the east and low A1/A amplitudes to the west, approximately follows the outline of the subducting Yakutat slab (Fig. 5). The contrast also broadly follows the terrane boundary between ANA to the east and AAT to the west (Fig. 2). Low amplitudes continue to the southwest along the projection of the Lake Clark fault, west to the coast, and north across the Seward Peninsula and the Brooks Range, as well as partially into the west-central Brooks Range (compare Figs. 1 and 5) across the western Alaskan and Arctic terranes. This region of western Alaska has a complex history involving the late Mesozoic evolution and amalgamation of Arctic Alaska–Chukotka microplates, subduction, extensive crustal thickening, arc plutonism, and sedimentation (Moore and Box, 2016; Till, 2016). Interestingly, $A1_{max}$ strikes vary somewhat systematically across the southern part of the Arctic Alaska terrane, with more west–east strikes across the northern Brooks Range toward the North Slope and more north-northwest–south-southeast strikes across the Seward Peninsula. The latter are similar to north-northwest–south-southeast to north-northeast–south-southwest strikes in the adjacent northern Koyukuk arc terrane (Fig. 2). To the extent that the generally north–south-trending topography reflects the tectonic grain in the northern Koyukuk region, $A1_{max}$ strikes indicate a moderate-to-deep signal that follows a distinctive grain in the orogen. These apparent orientation discontinuities may indicate that the Seward Peninsula and northern Koyukuk terrane were less affected by generally north–south-directed contraction that should produce more west–east fabrics and, thus, might represent the preservation of older, precollisional fabrics within the composite microplates. High-amplitude A1/A in the northwesternmost corner of Arctic Alaska is an interesting anomaly, as it has a north-northeast trend that is at high angles to the strikes of $A1_{max}$ in the surrounding region (compare Figs. 2 and 5).

Along the active, transpressional plate boundary in south-central Alaska, the accreted terranes, volcanic arc, and modern subduction zone, all show a large A1/A signal (Fig. 5) and a wide range of depths for $A1_{max}$ arrivals (Fig. 6a). Deep, possibly subcrustal $A1_{max}$ arrivals are concentrated from the Kenai Peninsula north under the Yakutat slab, in the area of maximum A1/A lithospheric average extending north to the Northern Foothills fold and thrust belt. The subcrustal arrivals may be related to the subducting slab, which has been imaged previously in common point conversion stacks and migrations of receiver functions (Ferris *et al.*, 2003; Ai *et al.*, 2005; Rossi *et al.*, 2006; Rondenay *et al.*, 2008, 2010; Kim *et al.*, 2014; Allam *et al.*, 2017). The $A1_{max}$ strikes of those deep arrivals are scattered to some extent, but they generally trend more north–south in regions that overlie the Pacific slab, such as the Kenai Peninsula, Kodiak Island, and Cook Inlet (Fig. 6a). The strikes are more northeast–southwest to the north in the region near the Denali fault that is above the projected edge of the Yakutat shallow slab. Depths of those arrivals are shallower than the modeled slab interface, but they tend to show similar strikes throughout the crust and into the mantle. We interpret this pattern to represent contractional structures above the slab that extend from shallow through plastic depths.

The analysis of $A1_{max}$ strikes in Figure 8 allows inferences related to fabrics near major faults as well as within blocks away from faults. The Tintina–Kaltag and Denali faults are subparallel along their west and east segments, and both show co-orientation with a large proportion of $A1_{max}$ strikes within a corridor ~30 km on both sides of the faults (Fig. 8b,c). This is particularly true for the eastern segments of these faults in which $A1_{max}$ orientations are also more densely sampled. The latter show a broad range of co-oriented moderate to shallow $A1_{max}$ depths. A small number of A1 strikes are also collocated with the fault traces for Kaltag and Denali west, although from moderate depths. West–east-oriented A1 strikes along the central Denali and Hines Creek fault segments are well represented and show the largest depth ranges and total depths along these faults (Fig. 8c). This may in part be due to station density variations, but it is also consistent with this portion of the fault zone having the greatest exhumation and

among the highest topography in the region adjacent to the Denali massif. This pattern may reflect deeply rooted plutonic or solid-state crustal fabrics that are now closer to the surface (compare with Benowitz *et al.*, 2011).

Station data selected from the intrafault blocks between Kaltag–Tintina and Denali (Fig. 8d,e) that do not include near-fault stations in Figure 8b,c show significant differences in orientation and depth distributions. $A1_{max}$ strikes in the eastern and western intra-Kaltag and Denali fault blocks are strongly co-oriented with the traces of each of the faults and are deepest with the broadest range in the western block (Fig. 8d). A moderate proportion of the signal is also parallel to the seismic zones and northeast fault lineaments thought to accommodate intrablock rotations (e.g., Page *et al.*, 1995), with generally shallower $A1_{max}$. In the eastern Tintina–Denali intrafault block, the dominant $A1_{max}$ strikes are not co-oriented with the fault traces, nor are the major A1 strikes shared with the western intrafault block (compare with Fig. 8d,e). The depth distribution in the eastern block (Fig. 8e) is also generally shallower than for the western block (Fig. 8d), which is characterized by a broad range of signal depths. The eastern intrafault block hosts some of the oldest metamorphic, solid-state fabrics (crystal-plastic deformation) in the YTT and NCO. The lack of co-orientation and collocation of intrafault block fabrics with the major fault traces may thus distinguish the older solid-state fabrics from younger, moderately shallow (and presumably brittle regime) near-fault fabrics (Fig. 8c) that have $A1_{max}$ co-oriented and collocated with the Denali east fault trace. This is consistent with a lack of an influence of younger deformation within the block from the eastern Tintina and Denali fault traces, compared to the western Kaltag and Denali fault traces that are strongly co-oriented and collocated with along-fault and intrablock $A1_{max}$ over a broad range of depths (Fig. 8d).

The fabrics in the intrafault block between the KMF and Kaltag faults represent components of the Arctic Alaska and Koyukuk terranes from the Seward Peninsula into western, interior Alaska (Fig. 2). The $A1_{max}$ fabrics here are unique, having north-northwest–south-southeast components that are not found in adjacent terranes, are from significant depth, and are not co-oriented with the traces of block-bounding faults (Fig. 8f). Moderately deep-to-shallow $A1_{max}$ signal is parallel to the KMF (subparallel to the Kaltag fault) in both the Seward Peninsula–Koyukuk block (Fig. 8f) and also at stations north of the KMF (Fig. 8g) representative of the Arctic Alaska terrane and Brooks Range. The predominantly northeast–southwest orientations of $A1_{max}$ are subparallel to the KMF, and they are also parallel to the overall geologic grain and topography of the Brooks Range and subparallel to other fabrics of the western portion of the other major NCO terranes. However, the north-northwest–south-southeast $A1_{max}$ orientations found in the Seward Peninsula–Koyukuk region (Fig. 8f) are not shared with Arctic Alaska of the Brooks Range (Fig. 8g). Thus, they may represent the pre-accretionary, possibly deeper fabric of a rotated fragment of the Arctic Alaska terrane.

The lithosphere-integrated A1/A amplitude (Fig. 5) is stronger near the plate margin and weaker in the interior. Seismicity that is coincident with fault lineaments appears to overlap with areas of low A1/A adjacent to the higher-amplitude areas that are also actively deforming (e.g., Minto seismic zone and vicinity, Fig. 9; Tape *et al.*, 2015). The relatively discrete lineaments and associated geology indicate that these features have small displacements and that some have sinistral strike-slip kinematics (Page *et al.*, 1995). These lineaments are less likely to have a strong fabric, material contrasts, and dip sufficient to generate a high-amplitude A1/A signal, perhaps because of the relatively small displacements or lack of juxtaposition of units with significant contrast.

$A1_{max}$ strikes do appear to align locally with structural features such as faults, folds, and material contrasts, even in such actively deforming areas that show low-integrated A1/A amplitude. The depth-integrated A1/A is, thus, an indicator that appears to track with structural intensity (i.e., the number of dipping faults, folds, and interfaces within an area or region) that is higher near the plate boundary in southern Alaska and diminishes to the north. In particular, the area of present-day subduction and active deformation associated with the projected Yakutat flat slab appear to correlate well with high-amplitude A1/A (Fig. 5). Elevated A1/A amplitudes near the westernmost and easternmost parts of the Brooks Range may coincide with regions of modern seismicity (Ruppert and West, 2019), although the general correlation between A1/A and seismicity is not high (e.g., the Seward Peninsula has seismicity but low integrated A1/A amplitude). However, a band of seismicity bisecting the Brooks Range in its center (Ruppert and West, 2019) may correlate with the transition from low to elevated A1/A in that area.

In most areas, we do not observe $A1_{max}$ strikes that show a clear change from one consistent orientation at shallow depths to a different consistent orientation at depths below the brittle-plastic transition. There may be a hint of depth-dependent behavior with strike in the area of the Yakutat flat slab, with deeper $A1_{max}$ strikes that are more parallel to slab depth contours than shallower $A1_{max}$ strikes (Fig. 5). Across all of Alaska, though, $A1_{max}$ strikes from different depths do appear to be more similar than not within the observed scatter (Fig. 8). This observation is significant because fabric at depths below the brittle crust may reflect recent solid-state deformation, whereas anisotropy within the brittle crust is less likely to result from solid-state deformation and associated crystallographic preferred orientation (CPO) from present-day deformation.

Accordingly, shallow crustal anisotropy is commonly interpreted to reflect the present-day stress state via the formation of fractures parallel to the maximum horizontal compressional stress. This interpretation is used in local shear-wave splitting studies, although significant deviations from this mechanism

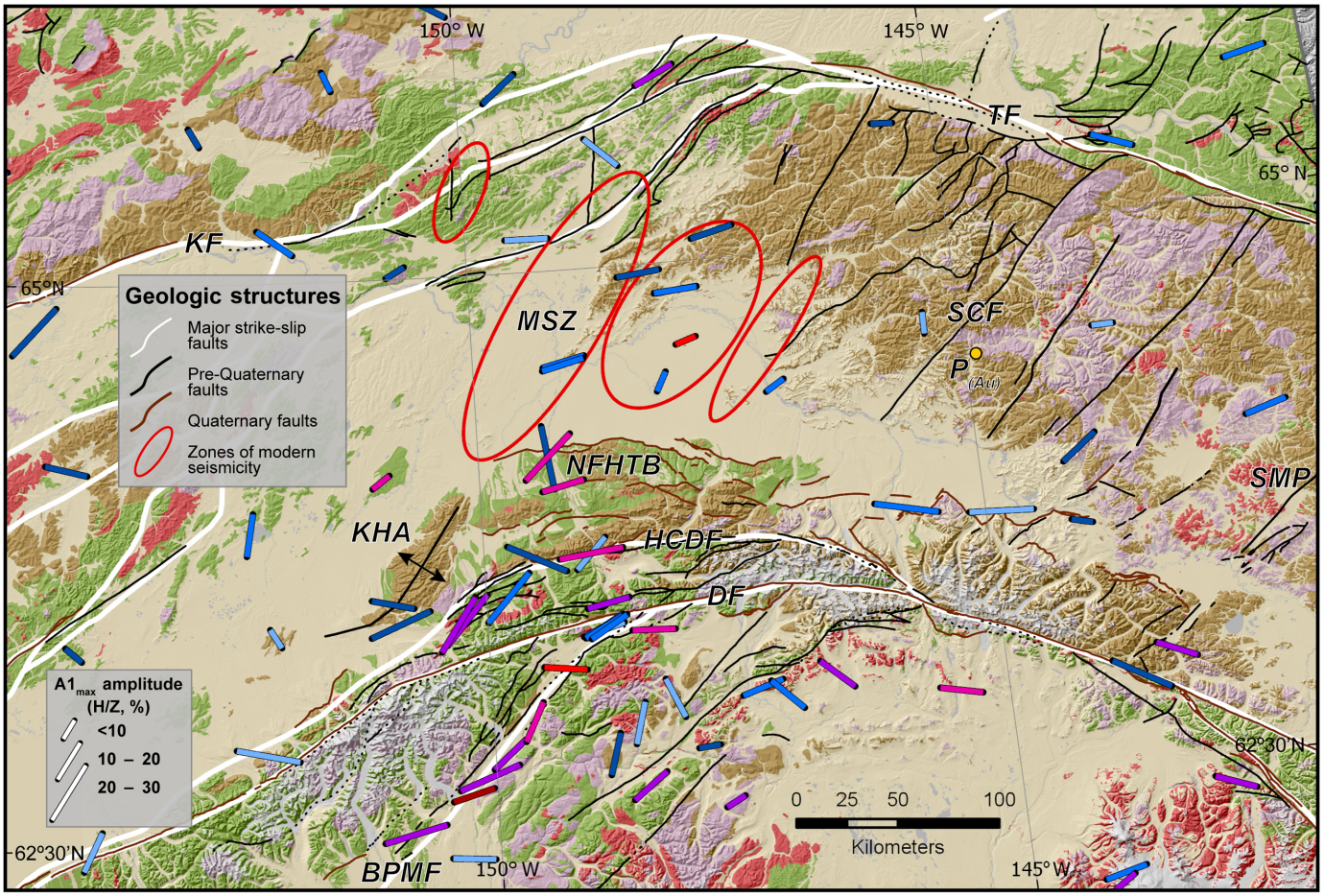

Figure 9. As in Figure 6a (including lengths and depth colors), but more detailed view of the Denali–Tintina area (outline in Fig. 1). Background is simplified geology, as in Figure 3. White fault traces are major strike-slip structures; black fault traces are pre-Quaternary structures from Plafker and Berg (1994), Koehler *et al.* (2013), and modified from Colpron and Nelson (2011); and other fault traces are Quaternary structures from Koehler *et al.* (2012). Feature names are the same as Figure 2, with the addition of BPMF, Broad Pass-Mulchatna; HCDF, Hines Creek strand of the Denali fault, Wahrhaftig *et al.* (1975); KHA, Kantishna Hills anticline; NFHTB, Northern Foothills fold and thrust belt of Bemis *et al.* (2015); SCF, Shaw Creek; and SMP, Sixtymile–Pika lineament. Ellipses are zones of modern-day seismicity from Koehler *et al.* (2012) and include the Minto seismic zone (MSZ) of Tape *et al.* (2015). $P_{(Au)}$ shows the location of the structurally controlled Pogo gold mine. (Modified from Colpron and Nelson, 2011; Wilson *et al.*, 2015; and Cui *et al.*, 2017.) The color version of this figure is available only in the electronic edition.

have been observed in actively deforming areas (e.g., Li and Peng, 2017). It is unclear whether shallow crustal fracturing and faulting would generate significant A1 arrivals in our receiver function analysis because localized juxtaposition of contrasting materials would also be required. Fractures and faults may also align with preexisting CPO that was developed at and exhumed from larger depths (e.g., Rasolofosaon *et al.*, 2000), in which case they could deviate from the modern stress field. CPO is strongly mineralogy dependent (e.g., Bernard and Behr, 2017), and so it is not necessarily a clear indicator of coupled or decoupled deformation with depth in the lithosphere. As such, an observed change in the orientation of anisotropy may only reflect a change in mineralogy instead of decoupled deformation.

With these caveats, we note a regional consistency of $A1_{max}$ strike orientation from different depths (Fig. 8). This suggests that fabrics above and below the brittle-plastic transition as well as tectonic grain (e.g., dipping contractional structures; Fuis *et al.*, 2008, and references therein) evolved in a similar stress field over similar time scales. Possible explanations are that (1) older fabrics and grain are overprinted by younger collisional fabrics in a way that reorients $A1_{max}$ strikes in the upper crust and at actively deforming depths or (2) preexisting fabrics and grain and present-day deformation interact in a way that preserves similar alignments, perhaps through reactivation of the older fabrics or through some other mechanism. Finer-scale and more detailed studies are necessary to resolve this question. We show initial comparisons to other geophysical constraints (crustal surface-wave azimuthal anisotropy, Feng and Ritzwoller, 2019b; *SKS* splitting, 2020 update of

the compilation from Becker *et al.*, 2012 with Estève *et al.*, 2020 and McPherson *et al.*, 2020; World Stress Map indicators, Heidbach *et al.*, 2018; moment tensors, Dziewonski *et al.*, 1981 and Ekström *et al.*, 2012; Kostrov summed as in Becker *et al.*, 2018; and geodetic strain rates, Kreemer *et al.*, 2014) in the supplemental material but leave further quantitative analysis for later.

Our results offer indirect insight into strain distribution laterally and with depth in the crust and lithosphere. The strong gradient in A1/A (Fig. 5) and $A1_{max}$ amplitudes (Fig. 7b) seen from the modern convergent boundary to the north suggests that our observations may reflect structural intensity, as defined previously, particularly in thrust belts such as the Chugach–St. Elias and Northern Foothills and within the megathrust and flat-slab subduction environments. In these areas, the $A1_{max}$ signal appears particularly strong at shallow depths, possibly indicating brittle failure, displacement, and deformation in the shallow crust that generates stronger fabrics and dipping isotropic contrasts. These features are distinct in comparison to those created by thermally activated, solid-state deformation fabric development in deeper and thickened crust and in places in the mantle wedge. Excursions of contractional deformation away from the active margin (i.e., Northern Foothills fold and thrust belt) are associated with the Yakutat flat slab and extend into the plastic crust (deeper $A1_{max}$ in Fig. 9, also Fig. 5). Weaker structural intensity in the interior is observed at the surface and reflected in low A1/A amplitudes. These observations do not preclude stress transmission into the interior, but, they can be consistent with subhorizontal fabric, because horizontal foliation does not generate a strong A1 signal (Schulte-Pelkum and Mahan, 2014a,b; Brownlee *et al.*, 2017). We interpret our observations of strong A1 signal as a reflection of high structural intensity possibly resulting from high-strain rates. Possible correlations to stress and the geographical distribution of microseismicity (Ruppert and West, 2019) are unclear. High A1/A in the south correlates geographically with seismicity, and one may speculate about a correlation for features in A1/A amplitude and microseismicity such as a northeast–southwest band crossing the Brooks Range, but low A1/A areas such as the Seward Peninsula also show seismicity.

Some trends in A1/A depth-integrated anisotropy appear to follow simplified terrane boundaries, but there is no clear correspondence between A1/A or $A1_{max}$ and lithology. Anisotropy does not only just depends on lithology but also on the strength of fabric within a given lithology. The probability of whether an A1 signal will be observed at a given station also depends on whether the fabric is broadly distributed across a unit or localized in narrow shear zones or other narrow geologic features. In the latter case, the signal is sensitive to the position of the station relative to localized structures. Our findings show that many $A1_{max}$ strikes are aligned with nearby structural trends, and that the $A1_{max}$ strike or amplitude does not necessarily change with distance from major faults. Thus, we suggest that the underlying tectonic grain in Alaska, and, by inference, the NCO, is broadly distributed, rather than strongly localized. In some areas, the tectonic grain is aligned with prominent metallogenic belts (Figs. 9 and 10), raising the possibility that mineral deposits in the region may be influenced by fabric trends that project from the upper crust to much greater depths.

Conclusions

We fit the first back-azimuthal harmonic of receiver function amplitudes in Alaska and interpret this signal as arising from contrasts in dipping foliation or other geological interfaces. We observe deep crustal signatures of tectonic grain (strikes parallel to mapped structural features) and volcanism (concentric strikes at modern volcanoes). No clear differences between receiver function signals from brittle versus plastic deformation depths are seen, suggesting coherence of deformation or fabric between these two domains. An exception may be the signal from slab depths versus the shallower lithosphere in the vicinity of the Yakutat flat-slab subduction. Elsewhere, the correspondence between shallow- and deep-fabric strikes suggests a similar degree of overprinting in the shallow and deep crust, in response to current strain. Strong deep fabric is concentrated in the current convergent plate boundary in which present-day strain rates are large, and fabric is weak in areas where major deformation is Mesozoic of age or older.

Data and Resources

Data used are available at DOI: 10.7914/SN/TA for the Transportable Array, DOI: 10.7914/SN/AK for the Alaska Regional Network, DOI: 10.7914/SN/AV for the Alaska Volcano Observatory, DOI: 10.7914/SN/CN for the Canadian National Seismic Network, DOI: 10.7914/SN/XE_1999 for the Broadband Experiment Across the Alaska Range (BEAAR) experiment, and DOI: 10.7914/SN/XR_2004 for the Observational and Theoretical Constraints on the Structure and Rotation of the Inner Core (ARCTIC) experiment. The facilities of Incorporated Research Institutions for Seismology (IRIS) Data Services, and specifically the IRIS Data Management Center, were used for access to waveforms and related metadata used in this study. Data were retrieved and preprocessed using Standing Order for Data (SOD; Owens *et al.*, 2004). Circular histograms were plotted with Orient (Vollmer, 2015). The supplemental material for this article includes comparison maps with other geophysical-oriented quantities, waveform plots illustrating the receiver function analysis, maps testing for sediment reverberations, and tables with A1/A and $A1_{max}$ for each station.

Acknowledgments

The authors thank the field teams, engineers, and managers of the Transportable Array, Alaska Regional and Volcano Observatory, and Canadian National Seismic Networks as well as field teams and Principal Investigators (PIs) of the temporary experiments Broadband Experiment Across the Alaska Range (BEAAR;

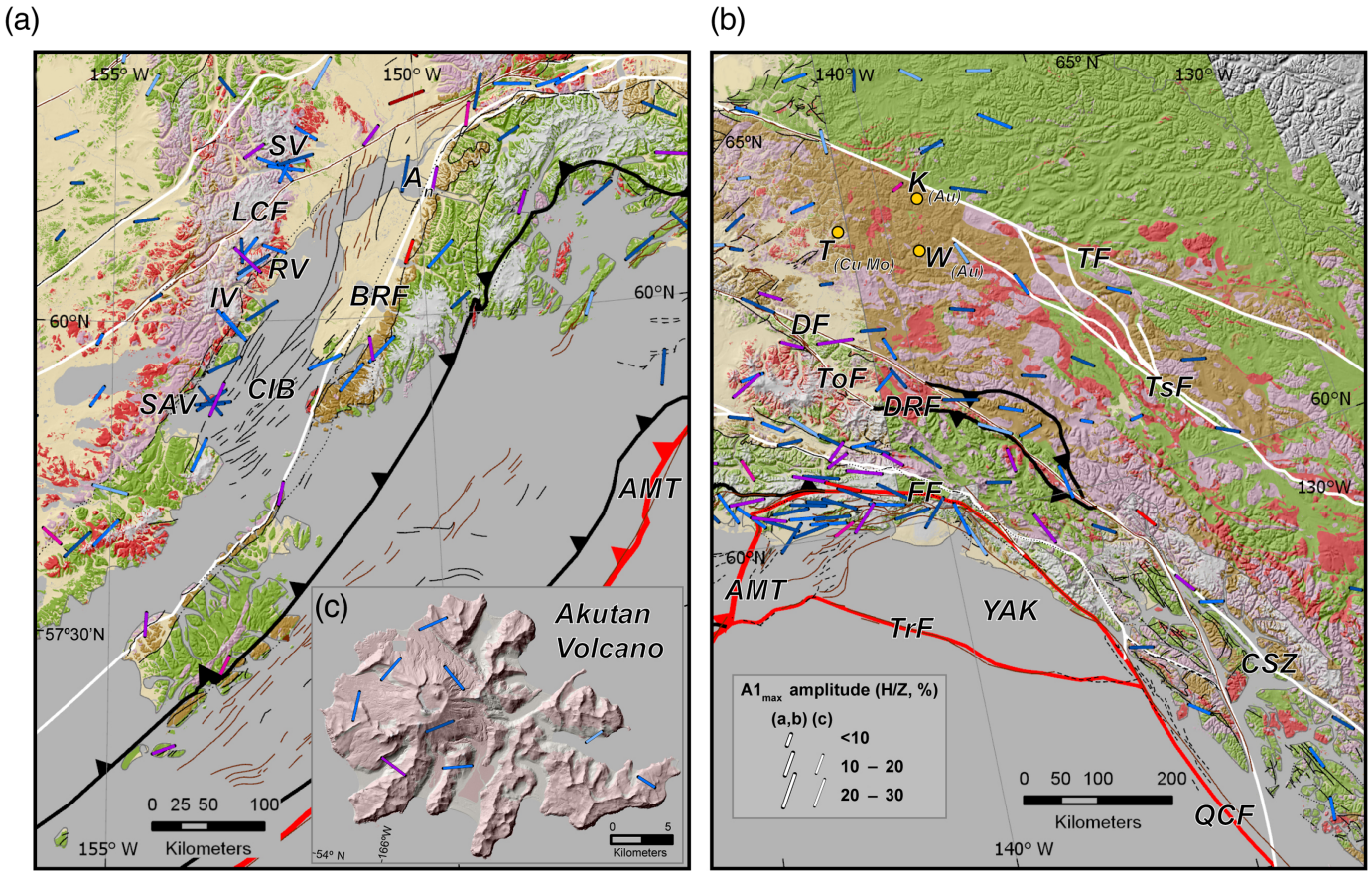

Figure 10. Detailed view of subparts of Figures 1 and 6a (including lengths and depth colors), background is geology, as in Figure 3. (a) Cook Inlet detailed view. Feature names are the same as Figure 2, with the addition of SV, RV, IV, SAV, which are volcanoes including Mounts Spurr, Redoubt, Illiamna, and Saint Augustine, respectively; An, Anchorage; CIB, Cook Inlet basin. (b) Indenter corner detailed view with additional feature names including bedrock mineral deposits showing primary metals; $K_{(Au)}$, Klondike veins; $T_{(Cu,Mo)}$, Taurus; $W_{(Au)}$, White Gold; YAK, Yakutat platform and microplate terrane; and faults CSZ, the Coast Range shear zone; DRF, Duke River; ToF, Totschunda; and TsF Teslin. (c) Inset shows a detailed view of an Aleutian Volcano (Akutan) shown in Figures 1 and 6a; scattered strikes near all volcanoes resolve into similar concentric patterns. (Modified from Colpron and Nelson, 2011; Wilson *et al.*, 2015; and Cui *et al.*, 2017.) The color version of this figure is available only in the electronic edition.

Christensen *et al.*, 1999) and Observational and Theoretical Constraints on the Structure and Rotation of the Inner Core (ARCTIC; Song and Christensen, 2004), as well as the Native corporations and First Nations that hosted seismic stations. Incorporated Research Institutions for Seismology (IRIS) Data Services are funded through the Seismological Facilities for the Advancement of Geoscience (SAGE) Award of the National Science Foundation (NSF) under Cooperative Support Agreement EAR-1851048. The authors thank Guest Editor Geoff Abers and reviewers Derek Schutt, Jens-Erik Lund Snee, and anonymous for suggestions that helped clarify and improve the article, and Lili Feng and Michael Ritzwoller for providing surface-wave results. Vera Schulte-Pelkum's contribution was funded by NSF Grants EAR-1927246, 1735890, and 1251193. Thorsten W. Becker was partially supported by EAR-1927216. U.S. Geological Survey (USGS), Mineral Resources Program supported Caine and Jones. Margaret Goldman and Keith Labay of the USGS are thanked for cartographic support. Any use of trade, firm, or product names is for descriptive purposes only and does not imply endorsement by the U.S. Government.

References

Ai, Y., D. Zhao, X. Gao, and W. Xu (2005). The crust and upper mantle discontinuity structure beneath Alaska inferred from receiver functions, *Phys. Earth Planet. In.* **150,** 339–350, doi: 10.1016/j.pepi.2004.12.002.

Allam, A. A., V. Schulte-Pelkum, Y. Ben-Zion, C. Tape, N. Ruppert, and Z. E. Ross, (2017). Ten kilometer vertical Moho offset and shallow velocity contrast along the Denali fault zone from double-difference tomography, receiver functions, and fault zone head waves, *Tectonophysics* **721,** 56–69, doi: 10.1016/j.tecto.2017.09.003.

Allan, M. M., J. K. Mortensen, C. J. R. Hart, L. A. Bailey, M. G. Sánchez, W. Ciolkiewicz, G. G. McKenzie, and R. A. Creaser (2013). Magmatic and metallogenic framework of west-central Yukon and Eastern Alaska, in *Tectonics, Metallogeny, And*

Discovery: The North American Cordillera and similar accretionary settings, M. Colpron, T. Bissig, B. Rusk, and J. Thompson (Editors) SEG, Denver, Colorado, Special Publication, Vol. 17, 111–168.

Amato, J. M., J. Toro, E. L. Miller, G. E. Gehrels, G. L. Farmer, E. S. Gottlieb, and A. B. Till (2009). Late Proterozoic–Paleozoic evolution of the Arctic Alaska–Chukotka terrane based on U-Pb igneous and detrital zircon ages: Implications for Neoproterozoic paleogeographic reconstructions, *Bull. Geol. Soc. Am.* **121**, 1219–1235, doi: 10.1130/B26510.1.

Barker, F., D. L. Jones, J. R. Budahn, and P. J. Coney (1988). Ocean plateau-seamount origin of basaltic rocks, Angayucham terrane, central Alaska, *J. Geol.* **96,** 368–374.

Becker, T. W., A. Hashima, A. M. Freed, and H. Sato (2018). Stress change before and after the 2011 M9 Tohoku-Oki earthquake, *Earth Planet Sci. Lett.* **504,** 174–184.

Becker, T. W., S. Lebedev, and M. D. Long (2012). On the relationship between azimuthal anisotropy from shear wave splitting and surface wave tomography, *J. Geophys. Res.* **117,** no. B01306, 1–17, doi: 10.1029/2011JB008705.

Bemis, S. P., R. J. Weldon, and G. A. Carver (2015). Slip partitioning along a continuously curved fault: Quaternary geologic controls on Denali fault system slip partitioning, growth of the Alaska Range, and the tectonics of south-central Alaska, *Lithosphere* **7,** 235–246, doi: 10.1130/L352.1.

Benowitz, J. A., P. W. Layer, P. Armstrong, S. E. Perry, P. J. Haeussler, P. G. Fitzgerald, and S. VanLaningham (2011). Spatial variations in focused exhumation along a continental-scale strike-slip fault: The Denali fault of the eastern Alaska Range, *Geosphere*, **7,** 455–467.

Beranek, L. P., C. R. van Staal, W. C. McClelland, N. Joyce, and S. Israel (2014). Late Paleozoic assembly of the Alexander–Wrangellia–Peninsular composite terrane, Canadian and Alaskan Cordillera, *Geol. Soc. Am. Bull.* **126,** 1531–1550.

Berg, E. M., F.-C. Lin, A. Allam, V. Schulte-Pelkum, K. M. Ward, and W. Shen (2020). Shear velocity model of Alaska via joint inversion of Rayleigh wave ellipticity, phase velocities, and receiver functions across the Alaska Transportable Array, *J. Geophys. Res.* **125,** e2019JB018582, doi: 10.1029/2019JB018582.

Bernard, R. E., and W. M. Behr (2017). Fabric heterogeneity in the Mojave lower crust and lithospheric mantle in southern California, *J. Geophys. Res.* **122,** 5000–5025, doi: 10.1002/2017JB014280.

Bradley, D. C., W. C. McClelland, R. M. Friedman, P. O'Sullivan, P. W. Layer, M. L. Miller, J. A. Dumoulin, A. B. Till, J. Grant Abbott, D. B. Bradley, and J. L. Wooden (2014). Proterozoic geochronological links between the Farewell, Kilbuck, and Arctic Alaska terranes, *J. Geol.* **122,** 237–258, doi: 10.1086/675663.

Brownlee, S. J., V. Schulte-Pelkum, A. Raju, K. Mahan, C. Condit, and O. F. Orlandini (2017). Characteristics of deep crustal seismic anisotropy from a compilation of rock elasticity tensors and their expression in receiver functions, *Tectonics* **36,** 1835–1857, doi: 10.1002/2017TC004625.

Bruhn, R. L., J. Sauber, M. M. Cotton, T. L. Pavlis, E. Burgess, N. Ruppert, and R. R. Forster (2012). Plate margin deformation and active tectonics along the northern edge of the Yakutat terrane in the Saint Elias orogen, Alaska, and Yukon, Canada, *Geosphere* **8,** 1384–1407.

2 Caine, J. S., and J. V. Jones III (2020). Exploring regional scale metamorphic fabrics in the Yukon Tanana terrane and environs using quantitative domain analyses, *Cordilleran Tectonics Workshop Program and Abstracts*, Anchorage, Alaska, 11–13.

Christensen, D., R. Hansen, and G. Abers (1999). *Broadband Experiment across the Alaska Range*, International Federation of Digital Seismograph Networks, Dataset/Seismic Network, doi: 10.7914/SN/XE_1999.

Christensen, N. I., and W. Mooney (1995). Seismic velocity structure and composition of the continental crust: A global view, *J. Geophys. Res.* **100,** 9761–9788, doi: 10.1029/95JB00259.

Colpron, M., and J. L. Nelson (2009). A Palaeozoic Northwest Passage: Incursion of Caledonian, Baltican and Siberian terranes into eastern Panthalassa, and the early evolution of the North American Cordillera, *Geol. Soc. Lond. Spec. Publ.* **318,** 273–307, doi: 10.1144/SP318.10.

Colpron, M., and J. L. Nelson (2011). A digital atlas of terranes for the northern Cordillera, *Yukon Geol. Surv.*, available at http://data.geology.gov.yk.ca/Compilation/2 (last accessed April 2020).

Colpron, M., J. L. Nelson, and D. C. Murphy (2007). Northern Cordilleran terranes and their interactions through time, *GSA Today* **17,** 4–7.

Coney, P. J., D. L. Jones, and J. W. H. Monger (1980). Cordilleran suspect terranes, *Nature* **288**, no. 7, 329–333.

Cui, Y., D. Miller, P. Schiarizza, and L. J. Diakow (2017). British Columbia Digital Geology, *British Columbia Geol. Surv. Open-File Rept. 2017-8*, British Columbia Ministry of Energy, Mines and Petroleum Resources, Victoria, Canada, 9 p. Data version 2019-12-19.

DeMets, C., R. G. Gordon, and D. F. Argus (2010). Geologically current plate motions, *Geophys. J. Int.* **181,** 1–180, doi: 10.1111/j.1365-246X.2009.04491.x.

Dusel-Bacon, C., M. J. Hopkins, J. K. Mortensen, S. S. Dashevsky, J. R. Bressler, and W. C. Day (2006). Paleozoic tectonic and metallogenic evolution of the pericratonic rocks of east-central Alaska and adjacent Yukon, in *Paleozoic Evolution and Metallogeny of Pericratonic Terranes at the Ancient Pacific Margin of North America, Canadian and Alaskan Cordillera*, M. Colpron and J. L. Nelson (Editors), Geological Association of Canada, St. Johns, Canada, Special Paper 45, 25–74.

Dziewonski, A. M., T.-A. Chou, and J. H. Woodhouse (1981). Determination of earthquake source parameters from waveform data for studies of global and regional seismicity, *J. Geophys. Res.* **86,** 2825–2852.

Eberhart-Phillips, D., D. H. Christensen, T. M. Brocher, R. Hansen, N. A. Ruppert, P. J. Haeussler, and G. A. Abers (2006). Imaging the transition from Aleutian subduction to Yakutat collision in central Alaska, with local earthquakes and active source data, *J. Geophys. Res.* **111,** 1–31, doi: 10.1029/2005JB004240.

Eisbacher, G. H. (1976). Sedimentology of the Dezadeash flysch and its implications for strike-slip faulting along the Denali fault, Yukon Territory and Alaska, *Can. J. Earth Sci.* **13,** 1495–1513, doi: 10.1139/e76-157.

Eisbacher, G. H. (1985). Pericollisional strike-slip faults and synorogenic basins, Canadian Cordillera, in *Strike-Slip Deformation, Basin Formation, and Sedimentation*, K. T. Biddle and N. Christie-Blick (Editors), SEPM Society for Sedimentary Geology, Tulsa, Oklahoma, doi: 10.2110/pec.85.37.0227.

Ekström, G., M. Nettles, and A. M. Dziewonski (2012). The Global CMT Project 2004–2010: Centroid-moment tensors for 13,017

earthquakes, *Phys. Earth Planet. In.* **200/201**, 1–9, doi: 10.1016/j.pepi.2012.04.002.

Enkelmann, E., J. I. Garver, and T. L. Pavlis (2008). Rapid exhumation of ice-covered rocks of the Chugach-St. Elias orogen, southeast Alaska, *Geology* **36,** 915–918, doi: 10.1130/G2252A.1.

Enkelmann, E., P. O. Koons, T. L. Pavlis, B. Hallet, A. Barker, J. Elliott, J. I. Garver, S. P. S. Gulick, R. M. Headley, G. L. Pavlis, *et al.* (2015). Cooperation among tectonic and surface processes in the St. Elias Range, earth's highest coastal mountains, *Geophys. Res. Lett.* **42,** 5838–5846, doi: 10.1002/2015GL064727.

Enkelmann, E., P. K. Zeitler, T. L. Pavlis, J. I. Garver, and K. D. Ridgway (2009). Intense localized rock uplift and erosion in the St. Elias orogen of Alaska, *Nature Geosci.* **2,** 360–636.

Estéve, C., P. Audet, A. J. Schaeffer, D. L. Schutt, R. C. Aster, and J. F. Cubley (2020). Seismic evidence for craton chiseling and displacement of lithospheric mantle by the Tintina fault in the northern Canadian Cordillera, *Geology* **48,** doi: 10.1130/G47688.1.

Feng, L., and M. H. Ritzwoller (2019a). A 3-D shear velocity model of the crust and uppermost mantle beneath Alaska including apparent radial anisotropy, *J. Geophys. Res.* **124,** 10,468–10,497, doi: 10.1029/2019JB018122.

Feng, L., and M. H. Ritzwoller (2019b). Radial and azimuthal anisotropy of the crust and uppermost mantle beneath Alaska inferred from surface waves, *Eos Trans. AGU* S41D-0549, 2019AGUFM.S41D0549L.

Ferris, A., G. A. Abers, D. H. Christensen, and E. Veenstra (2003). High resolution image of the subducted Pacific (?) plate beneath central Alaska, 50–150 km depth, *Earth Planet. Sci. Lett.* **214,** 575–588, doi: 10.1016/S0012-821X(03)00403-5.

Fuis, G., T. Moore, G. Plafker, T. Brocher, M. Fisher, W. Mooney, W. Nokleberg, R. Page, B. Beaudoin, N. Christensen *et al.* (2008). Trans-Alaska Crustal Transect and continental evolution involving subduction underplating and synchronous foreland thrusting, *Geology* **36,** 267–270, doi: 10.1130/G24257A.1.

Gabrielse, H., D. C. Murphy, and J. K. Mortensen (2006). Cretaceous and Cenozoic dextral orogen-parallel displacements, magmatism, and paleogeography, north-central Canadian Cordillera, in *Paleogeography of the North American Cordillera: Evidence For and Against Large-Scale Displacements*, J. W. Haggart, R. J. Enkin, and M. J. W. H. (Editors), Geological Association of Canada, St. Johns, Canada, 255–276.

Glen, J. M. G. (2004). A kinematic model for the southern Alaska orocline based on regional fault patterns, in *Geological Society of America Special Paper 383*, A. J. Sussman and A. B. Weil (Editors), Boulder, Colorado, 161–172.

Grantz, A., S. D. May, and P. E. Hart (1994). Geology of the Arctic continental margin of Alaska, in *The Geology of Alaska*, G. Plafker and H. C. Berg (Editors), Geological Society of America, Boulder, Colorado, 17–48, doi: 10.1130/DNAG-GNA-G1.17.

Grantz, A., R. A. Scott, S. S. Drachev, T. E. Moore, and Z. C. Valin (2011). Chapter 2: Sedimentary successions of the Arctic region (58–64° to 90° N) that may be prospective for hydrocarbons, *Memoir Geol. Soc. Lond.* **35,** 17–37, doi: 10.1144/M35.2.

GTOPO 30 m DEM (2020). Digital elevation model from Airbus, USGFS NGA, NASA, CGIAR, NCEAS, NLS, OS, NMA, Geodatastyrelsen, GSA, and the GIS User *Community*, available at https://www.usgs.gov/centers/eros/science/usgs-eros-archive-digital-elevation-global-30-arc-second-elevation-gtopo30?qt-science_center_objects=0#qt-science_center_objects (last accessed April 2020).

Haeussler, P. J., D. C. Bradley, R. E. Wells, and M. L. Miller (2003). Life and death of the Resurrection plate: Evidence for its existence and subduction in the northeastern Pacific in Paleocene–Eocene time, *Geol. Soc. Am. Bull.* **115,** no. 7, 867–880, doi: 10.1130/0016-7606(2003)115< 0867:LADOTR>2.0.CO;2.

Hayes, G. P., D. J. Wald, and R. L. Johnson (2012). Slab1.0: A three-dimensional model of global subduction zone geometries, *J. Geophys. Res.* **117,** no. B01302, 1–15, doi: 10.1029/2011JB008524.

Heidbach, O., M. Rajabi, X. Cui, K. Fuchs, B. Müller, J. Reinecker, K. Reiter, M. Tingay, F. Wenzel, F. Xie, *et al.* (2018). The World Stress Map database release 2016: Crustal stress pattern across scales, *Tectonophysics* **744**, 484–498.

Janiszewski, H. A., G. A. Abers, D. J. Shillington, and J. A. Calkins (2013). Crustal structure along the Aleutian island arc: New insights from receiver functions constrained by active-source data, *Geochem. Geophys. Geosyst.* **14,** 2977–2992, doi: 10.1002/ggge.20211.

Janiszewski, H. A., L. S. Wagner, and D. C. Roman (2020). Aseismic mid-crustal magma reservoir at Cleveland Volcano imaged through novel receiver function analyses, *Sci. Rep.* **10,** 1780, doi: 10.1038/s41598-020-58589-0.

Ji, S., T. Shao, K. Michibayashi, C. Long, Q. Wang, Y. Kondo, W. Zhao, H. Wang, and M. H. Salisbury (2013). A new calibration of seismic velocities, anisotropy, fabrics, and elastic moduli of amphibole-rich rocks, *J. Geophys. Res.* **118,** 4699–4728, doi: 10.1002/jgrb.50352.

Jicha, B. R., D. W. Scholl, B. S. Singer, G. M. Yogodzinski, and S. M. Kay (2006). Revised age of Aleutian island arc formation implies high rate of magma production, *Geology* **34,** 661–664.

Jones, C., and R. Phinney (1998). Seismic structure of the lithosphere from teleseismic converted arrivals observed at small arrays in the southern Sierra Nevada and vicinity, California, *J. Geophys. Res.* **103,** 10,065–10,090.

Kim, Y., G. A. Abers, J. Li, D. Christensen, J. Calkins, and S. Rondenay (2014). Alaska Megathrust 2: Imaging the megathrust zone and Yakutat/Pacific plate interface in the Alaska subduction zone, *J. Geophys. Res.* **119,** 1924–1941, doi: 10.1002/2013JB010581.

Koehler, R. D., P. A. C. Burns, and J. R. Weakland (2013). *Digitized Faults of the Neotectonic Map of Alaska (Plafker and others, 1994)*, Alaska Division of Geological & Geophysical Surveys, Fairbanks, Alaska, Miscellaneous Publication 150, doi: 10.14509/24791.

Koehler, R. D., R.-E. Farrell, P. A. C. Burns, and R. A. Combellick (2012). Quaternary faults and folds in Alaska: A digital database, in *Quaternary Faults and Folds (QFF)*, R. D. Koehler (Editor), Alaska Division of Geological & Geophysical Surveys, Fairbanks, Alaska, Miscellaneous Publication 141, 31 p., 1 sheet, scale 1:3,700,000, doi: 10.14509/23944.

Koons, P. O., B. P. Hooks, T. Pavlis, P. Upton, and A. D. Barker (2010). Three-dimensional mechanics of Yakutat convergence in the southern Alaskan plate corner, *Tectonics* **29,** doi: 10.1029/2009TC002463.

Kreemer, C., G. Blewitt, and E. C. Klein (2014). A geodetic plate motion and global strain rate model, *Geochem. Geophys. Geosyst.* **15,** 3849–3889, doi: 10.1002/2014GC005407.

Leonard, L. J., R. D. Hyndman, S. Mazzotti, L. Nykolaishen, M. Schmidt, and S. Hippchen (2007). Current deformation in the northern Canadian Cordillera inferred from GPS measurements, *J. Geophys. Res.* **112,** 1–15, doi: 10.1029/2007JB005061.

Lepain, D. L., R. G. Stanley, K. P. Helmold, and D. P. Shellenbaum (2013). Geologic framework and petroleum systems of Cook Inlet Basin, South-Central Alaska, in *Oil and Gas Fields of the Cook Inlet Basin, Alaska*, D. M. Stone and D. M. Hite (Editors), Vol. 104, AAPG Memoir, Tulsa, Oklahoma, 37–116.

Levin, V., and J. Park (1998). *P-SH* conversions in layered media with hexagonally symmetric anisotropy: A cookbook, *Pure Appl. Geophys.* **151,** 669–697.

Li, Z., and Z. Peng (2017). Stress- and structure-induced anisotropy in southern California from two decades of shear wave splitting measurements, *Geophys. Res. Lett.* **44,** no. 19, 9607–9614, doi: 10.1002/2017GL075163.

Ligorria, J., and C. Ammon (1999). Iterative deconvolution and receiver-function estimation, *Bull. Seism. Soc. Am.* **89,** no. 5, 1395–1400.

Mair, J. L., G. L. Farmer, D. I. Groves, C. J. R. Hart, and R. J. Goldfarb (2011). Petrogenesis of postcollisional magmatism at Scheelite Dome, Yukon, Canada: Evidence for a lithospheric mantle source for magmas associated with intrusion-related gold systems, *Econ. Geol.* **106,** 451–480, doi: 10.2113/econgeo.106.3.451.

McPherson, A. M., D. H. Christensen, G. A. Abers, and C. Tape (2020). Shear wave splitting and mantle flow beneath Alaska, *J. Geophys. Res.* **123,** e2019JB018329, doi: 10.1029/2019JB018329.

Miller, E. L., and T. L. Hudson (1991). Mid-Cretaceous extensional fragmentation of a Jurassic-early Cretaceous compressional orogen, Alaska, *Tectonics* **10,** 781–796.

Miller, E. L., K. E. Meisling, V. V. Akinin, K. Brumley, B. J. Coakley, E. S. Gottlieb, C. W. Hoiland, T. M. O'Brien, A. Soboleva, and J. Toro (2018). Circum-Arctic Lithosphere Evolution (CALE) transect C: Displacement of the Arctic Alaska–Chukotka microplate towards the Pacific during opening of the Amerasia basin of the Arctic, *Geol. Soc. Spec. Publ.* **460,** 57–120, doi: 10.1144/sp460.9.

Miller, M. L., D. C. Bradley, T. K. Bundtzen, and W. McClelland (2002). Late cretaceous through Cenozoic strike-slip tectonics of southwestern Alaska, *J. Geol.* 247–270.

Monger, J. W. H., and H. Daniel Gibson (2018). Mesozoic-Cenozoic deformation in the Canadian Cordillera: The record of a "Continental Bulldozer"? *Tectonophysics* **757,** 153–169, doi: 10.1016/j.tecto.2018.12.023.

Moore, T. E., and S. E. Box (2016). Age, distribution and style of deformation in Alaska north of 60°N: Implications for assembly of Alaska, *Tectonophysics* **691,** 133–170, doi: 10.1016/j.tecto.2016.06.025.

Moore, T. E., W. K. Wallace, K. J. Bird, S. M. Karl, C. G. Mull, and J. T. Dillon, (1994), Geology of northern Alaska, in *The Geology of Alaska*, G. Plafker and H. C. Berg (Editors), Geological Society of America, Boulder, Colorado, 49–140, doi: 10.1130/DNAG-GNA-G1.49.

Mortensen, J. K., C. J. R. Hart, D. C. Murphy, and S. Heffernan (2000). Temporal evolution of early and mid-Cretaceous magmatism in the Tintina gold belt, in *The Tintina gold belt; concepts, exploration, and discoveries*, T. L. Tucker and M. T. Smith (Editors), British Columbia and Yukon Chamber of Mines Cordilleran Roundup, Vancouver, British Columbia, Canada, Special Vol. 2, 49–58.

Murphy, D. C. (2018). Latest Cretaceous–early Eocene Pacific-Arctic?-Atlantic connection: Co-evolution of strike-slip fault systems, oroclines, and transverse fold-and-thrust belts in the northwestern North American Cordillera, in *Circum-Arctic Structural Events: Tectonic Evolution of the Arctic Margins and Trans-Arctic Links with Adjacent Orogens*, K. Piepjohn, J. V. Strauss, L. Reinhardt, and W. C. McClelland (Editors), Geological Society of America, Boulder, Colorado, Special Paper 541, 1–22.

Nelson, J. L., M. Colpron, and S. Israel (2013). The Cordillera of British Columbia, Yukon, and Alaska: Tectonics and metallogeny, in *Tectonics, Metallogeny, and Discovery: The North American Cordillera and Similar Accretionary Settings*, Society of Economic Geologists, Denver, Colorado, doi: 10.5382/SP.17.03.

O'Brien, T. M., E. L. Miller, V. Pease, L. A. Hayden, C. M. Fisher, J. K. Hourigan, and J. D. Vervoort (2018). Provenance, U-Pb detrital zircon geochronology, Hf isotopic analyses, and Cr-spinel geochemistry of the northeast Yukon–Koyukuk basin: Implications for interior basin development and sedimentation in Alaska, *Bull. Geol. Soc. Am.* **130,** nos. 5/6, 825–847, doi: 10.1130/B31825.1.

Owens, T. J., H. P. Crotwell, C. Groves, and P. Oliver-Paul (2004). SOD: Standing Order for Data, *Seismol. Res. Lett.* **75,** 515–520.

Page, R. A., G. Plafker, and H. Pulpan, (1995). Block rotation in east-central Alaska: A framework for evaluating earthquake potential? *Geology* **23,** 629–632.

Park, J., and V. Levin (2016). Anisotropic shear zones revealed by backazimuthal harmonics of teleseismic receiver functions, *Geophys. J. Int.* **207,** no. 2, 1216–1243, doi: 10.1093/gji/ggw323.

Patton, W. W., Jr. (1973). *Reconnaissance geology of the northern Yukon–Koyukuk Province, Alaska*, *U.S. Geol. Surv. Profess. Pap. 774-A*, 17.

Pavlis, L., V. B. Sisson, H. L. Foster, W. J. Nokleberg, and G. Plafker (1993) Mid-cretaceous extensional tectonics of the Yukon–Tanana terrane, Trans-Alaska Crustal Transect (TACT), east-central Alaska, *Tectonics*, **12,** 103–122, doi: 10.1029/92TC00860.

Pavlis, T. L., and S. M. Roeske (2007). The Border Ranges fault system, southern Alaska, in *Tectonic Growth of a Collisional Continental Margin: Crustal Evolution of Southern Alaska*, K. D. Ridgway, J. M. Trop, J. M. G. Glen, and J. M. O'Neill (Editors), Geological Society of America, Boulder, Colorado, Special Paper 431, 95–127, doi: 10.1130/2007.2431(05).

Pavlis, T. L., and V. B. Sisson (2003). Development of a subhorizontal decoupling horizon in a transpressional system, Chugach metamorphic complex, Alaska: Evidence for rheological stratification of the crust, *Geol. Soc. Am. Spec. Pap.* **371,** 191–216.

Pavlis, T. L., J. M. Amato, J. M. Trop, K. D. Ridgway, S. M. Roeske, and G. E. Gehrels (2019). Subduction polarity in ancient arcs: A call to integrate geology and geophysics to decipher the Mesozoic tectonic history of the northern Cordillera of North America, *GSA Today*, **29,** doi: 10.1130/GSATG402A.1.

Pease, V., and B. Coakley (2018). Circum-Arctic Lithosphere Evolution, *Geol. Soc. Lond. Spec. Publ.* **460,** 1–6, doi: 10.1144/sp460.19.

Plafker, G. (1987). Regional geology and petroleum potential of the northern Gulf of Alaska continental margin, in *Geology and Resource Potential of the Continental Margin of Western North*

America and Adjacent Ocean Basins—Beaufort Sea to Baja California, Earth Science Series, Vol. 6, Circum-Pacific Council for Energy and Mineral Resources, Houston, Texas, 229–268.

Plafker, G., and H. C. Berg (1994). Overview of the geology and tectonic evolution of Alaska, in *The Geology of North America*, G. Plafker and H. C. Berg (Editors), Vol. G-1, Boulder, Colorado, 989–1021.

Rasendra, N., M. Bonnin, S. Mazzotti, and C. Tiberi (2014). Crustal and upper-mantle anisotropy related to fossilized transpression fabric along the Denali fault, northern Canadian Cordillera, *Bull. Seismol. Soc. Am.* **104,** 1964–1975, doi: 10.1785/0120130233.

Rasolofosaon, P. N. J., W. Rabbel, S. Siegesmund, and A. Vollbrecht (2000). Characterization of crack distribution: Fabric analysis versus ultrasonic inversion, *Geophys. J. Int.* **141,** 413–424.

Reed, B. L., and M. A. Lanphere (1974). Offset plutons and history of movement along the McKinley segment of the Denali fault system, Alaska, *Bull. Geol. Soc. Am.* **85,** 1883–1892, doi: 10.1130/0016-7606(1974)85<1883:OPAHOM>2.0.CO;2.

Regan, S. P., J. A. Benowitz, and M. E. Holland (2020). A plutonic brother from another magma mother: Disproving the Eocene Foraker–McGonagall pluton piercing point and implications for long-term slip on the Denali fault, *Terra Nova* **32,** 66–74, doi: 10.1111/ter.12437.

Rondenay, S., G. A. Abers, and P. E. van Keken (2008). Seismic imaging of subduction zone metamorphism, *Geology* **36,** 275–278, doi: 10.1130/G24112A.1.

Rondenay, S., L. G. Montesi, and G. A. Abers (2010). New geophysical insight into the origin of the Denali Volcanic gap, *Geophys. J. Int.* **182,** 613–630, doi: 10.1111/j.1365-246X.2010.04659.x.

Rossi, G., G. A. Abers, S. Rondenay, and D. H. Christensen (2006). Unusual mantle Poisson's ratio, subduction, and crustal structure in central Alaska, *J. Geophys. Res.* **111,** no. B09311, doi: 10.1029/2005JB003956.

Ruppert, N. A., and M. E. West (2019). The impact of USArray on earthquake monitoring in Alaska, *Seismol. Res. Lett.* **91,** 601–610, doi: 10.1785/0220190227.

Sánchez, M. G., M. M. Allan, C. J. R. Hart, and J. K. Mortensen (2014). Extracting ore-deposit-controlling structures from aeromagnetic, gravimetric, topographic, and regional geologic data in western Yukon and eastern Alaska, *Interpretation* **2,** 75–102, doi: 10.1190/INT-2014-0104.1.

Savage, M. K. (1998). Lower crustal anisotropy or dipping boundaries: Effects on receiver functions and a case study in New Zealand, *J. Geophys. Res.* **103,** 15,069–15,087.

Schulte-Pelkum, V., and K. H. Mahan (2014a). A method for mapping crustal deformation and anisotropy with receiver functions and first results from USArray, *Earth Planet. Sci. Lett.* **402,** 221–233, doi: 10.1016/j.epsl.2014.01.050.

Schulte-Pelkum, V., and K. H. Mahan (2014b). Imaging faults and shear zones using receiver functions, *Pure Appl. Geophys.* **171,** 2967–2991, doi: 10.1007/s00024-014-0853-4.

Schulte-Pelkum, V., Z. Ross, K. Mueller, and Y. Ben-Zion (2020). Tectonic inheritance with dipping faults and deformation fabric in the brittle and ductile southern California crust, *J. Geophys. Res.* doi: 10.1029/2020JB019525.

Smith, W. H. F., and P. Wessel (1990). Gridding with a continuous curvature surface in tension, *Geophysics* **55,** 293–305.

Song, X., and D. Christensen (2004). *CSEDI: Observational and Theoretical Constraints on the Structure and Rotation of the Inner Core*, International Federation of Digital Seismograph Networks, Dataset/Seismic Network, doi: 10.7914/SN/XR_2004.

Strauss, J. V., F. A. Macdonald, J. F. Taylor, J. E. Repetski, and W. C. McClelland (2013). Laurentian origin for the North Slope of Alaska: Implications for the tectonic evolution of the Arctic, *Lithosphere* **5,** 477–482, doi: 10.1130/L284.1.

Syracuse, E. M., M. Maceira, H. Zhang, and C. H. Thurber (2015). Seismicity and structure of Akutan and Makushin Volcanoes, Alaska, using joint body and surface wave tomography, *J. Geophys. Res.* **120,** 1036–1052, doi: 10.1002/2014JB011616.

Tape, C., V. Silwal, C. Ji, L. Keyson, M. E. West, and N. Ruppert (2015). Transtensional tectonics of the Minto Flats fault zone and Nenana basin, central Alaska, *Bull. Seism. Soc. Am.* **105,** 2081–2100, doi: 10.1785/0120150055.

Templeman-Kluit, D. (1976). The Yukon crystalline terrane: Enigma in the Canadian Cordillera, *Geol. Soc. Am. Bull.* **87,** 1343–1357.

Till, A. B. (2016). A synthesis of Jurassic and early Cretaceous crustal evolution along the southern margin of the Arctic Alaska–Chukotka microplate and implications for defining tectonic boundaries active during opening of Arctic Ocean basins, *Lithosphere* **8,** 219–237, doi: 10.1130/L471.1.

Trop, J. M., J. Benowitz, R. B. Cole, and P. O. Sullivan (2019). Cretaceous to Miocene magmatism, sedimentation, and exhumation within the Alaska Range suture zone: A polyphase reactivated terrane boundary, *Geosphere* **15,** 1–36.

Vallier, T. L., D. W. Scholl, M. A. Fisher, T. R. Bruns, F. H. Wilson, R. von Huene, and A. J. Stevenson (1994). Geologic framework of the Aleutian Arc, Alaska, in *The Geology of North America*, G. Plafker and H. C. Berg (Editors), Vol. G-1, Geological Society of America, Boulder, Colorado, 367–388.

Vollmer, F. W. (2015). Orient 3: A new integrated software program for orientation data analysis, kinematic analysis, spherical projections, and Schmidt plots, *Geol. Soc. Am. Abstr. Progr.* **47,** no. 7, 49.

Wahrhaftig, C., D. L. Turner, F. R. Weber, and T. E. Smith (1975). Nature and timing of movement on Hines Creek strand of Denali fault system, Alaska, *Geology* **3,** 463–466.

Wilson, C. K., C. H. Jones, and H. J. Gilbert (2003). Single-chamber silicic magma system inferred from shear wave discontinuities of the crust and uppermost mantle, Coso geothermal area, California, *J. Geophys. Res.* **108,** no. B5, 2226, doi: 10.1029/2002JB001798.

Wilson, F. H., C. P. Hults, C. G. Mull, and S. M. Karl (2015). *Geologic map of Alaska*, *U.S. Geol. Surv. Scientific Investigations Map 3340*, pamphlet, 196 p., 2 sheets, scale 1:1,584,000, doi: 10.3133/sim3340.

Yukon Geological Survey (2020). Yukon Digital Bedrock Geology, *Yukon Geol. Surv.*, available at http://datatest.geology.gov.yk.ca/Compilation/3 (last accessed April 2020).

Manuscript received 11 May 2020

Queries

1. AU: SSA tries to avoid using a slash in nonmathematical contexts. Please provide alternative wording for "deformation/dip", and "geologic/tectonic" in the article and artwork of Figure 6.
2. AU: Please provide conference date and month and URL address along with last accessed month and year for reference "Caine and Jones (2020)."
3. AU: Please update volume number, page range and DOI number for reference "Feng and Ritzwoller (2019b)."